Simulating Causes of Conductivity Degradation in Nanoscale Metal Wires

Baruch Feldman

A dissertation submitted in partial fulfillment
of the requirements for the degree of

Doctor of Philosophy

University of Washington

2008

Program Authorized to Offer Degree:
Physics

University of Washington
Graduate School

This is to certify that I have examined this copy of a doctoral dissertation by

Baruch Feldman

and have found that it is complete and satisfactory in all respects,
and that any and all revisions required by the final
examining committee have been made.

Chair of the Supervisory Committee:

_____

Scott T. Dunham

Reading Committee:

_____

Scott T. Dunham

_____

John Rehr

_____

Anton Andreev

Date: _____

University of Washington

Abstract

Simulating Causes of Conductivity
Degradation in Nanoscale Metal Wires

Baruch Feldman

Chair of the Supervisory Committee:
Professor Scott T. Dunham
Electrical Engineering Department

Nanowires made of metal, particulary copper, are increasingly important for interconnecting transistors in modern electronics. Nanowire conductance is known to degrade with decreasing thickness, but the microscopic causes of this are poorly understood.

This work presents calculations of conductivity degradation in nanowires due to scattering from surfaces, grain boundaries, and interfaces with liner layers. It studies the detailed effect of surface roughness profile, or power spectral density (PSD). It also presents the first fundamental calculations of transport across crystal grain boundaries and interfaces between copper and tantalum liner layers.

It is found that the components of surface roughness with shortest wavelengths have the greatest effect on conductivity, even when taking into account typical surface profile falloffs as a power law of wavelength. Furthermore, it is found that surface roughness is not an insurmountable barrier to conduction, with diffuse scattering probability $(1 - p) = 4\%$ for typical surface profiles. Grain boundaries are found to be important scattering sources, and less ordered grain boundaries, such as non-twin boundaries or those with defects, have greatly increased scattering. Finally, transmission from Cu to Ta is found to have probability $T = 22\%$, so nanowires surrounded by at least a few nm of Ta greatly degrade in conductivity. It is concluded that

grain boundaries and the liner layer interface are important sources of conductivity degradation.

TABLE OF CONTENTS

LIST OF FIGURES

iv

ACKNOWLEDGMENTS

Chapter 1

INTRODUCTION

The transistor devices that power the logic and computation in computers have, for decades, obeyed Moore's Law [54, 3]: the number of transistors in a computer processor doubles every two years, due mostly to a reduction in size of the transistor. As transistors have reached the nanoscale regime[1], they have begun to encounter a whole host of physical limitations on their ability to scale. One of these issues is that the nanoscale wires used to interconnect these transistors degrade in conductivity as they are made smaller. Several mechanisms have been proposed for the degradation, including grain boundary, surface, and interface scattering (see Figure 1.1). This thesis aims to predict these effects for the first time from fundamental physics, using both simulation and calculation.

1.1 Problems Caused by Conductivity Degradation

The conductivity degradation in nanoscale wires described above is substantial: it has been observed to be 50% or greater compared to bulk in nanoscale films and wires [56, 3, 20, 74, 75] (see Figure 1.2). This degradation causes various practical problems for semiconductor technology. It causes RC delays [60, 3] and power loss [3], problems which will be described further in the following sub-sections. These problems in turn limit the speed and battery life performance of the entire digital device.

---

[1]Defined loosely as a minimum feature size below 100 nm. At this writing, the generation of transistors in development has a minimum feature size of 32 nm, or about 100 times the size of a typical atom.
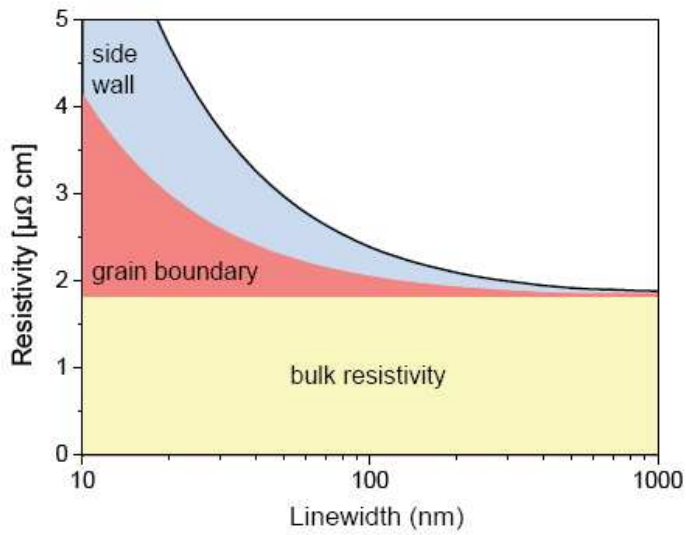
Figure 1.1: Imputed causes of conductivity degradation, from International Technology Roadmap for Semiconductors [3].
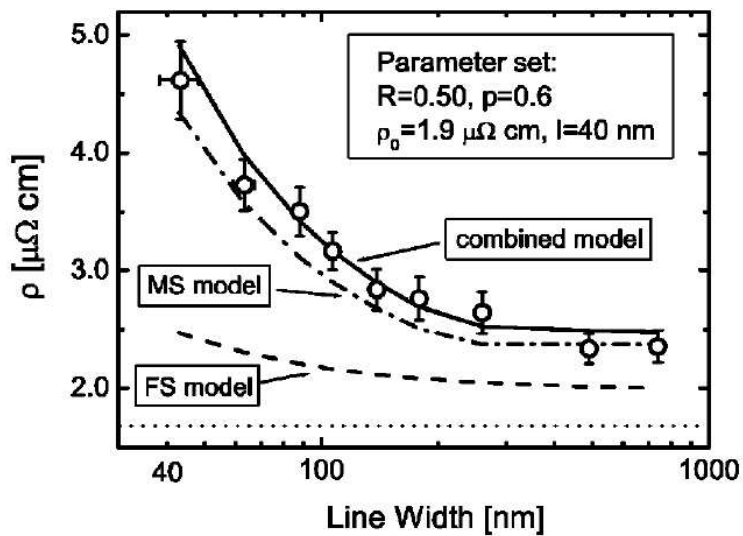
Figure 1.2: Resistivity as a function of thickness, together with fits to the Fuchs-Sondheimer and Mayadas-Shatzkes (see Chapter 2) semi-classical models of size effects. Figure is taken from [74].
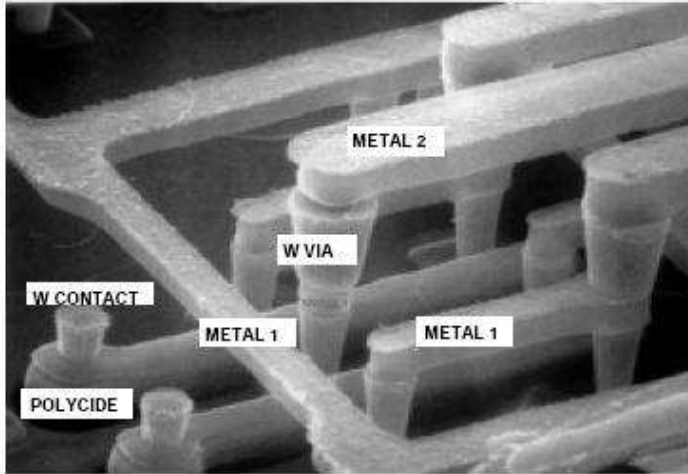
Figure 1.3: Layers of interconnect from a microprocessor with the SiO_2 substrate removed. Photo is from [60].

To illustrate the importance of interconnect conductivity, consider that in the late 1990s the semiconductor industry switched from aluminum interconnecting wires to copper. Although aluminum had previously been used for over 40 years because its desirable properties made it less expensive to deposit in a circuit [60], copper has 55% higher conductivity. Nevertheless, about 10 years later, the industry is again facing limits to performance due to conductivity as wires must be scaled ever smaller.

1.1.1 Back-End Technology

Current microprocessor technology is based on CMOS technology, a method to design all the elementary logical functions like AND, OR, and NOT out of transistors. In order to create the correct logical operations, the transistors must be interconnected appropriately. In modern integrated circuit technology, some 10^7 - 10^8 transistors are laid out on Si wafers. Making these transistors into logic and circuits requires billions of interconnections, made in 7 or more layers of metal wires known as **interconnects** or **back-end technology**. This is illustrated in Fig. 1.3.

These layers of interconnect form a complex network where the higher levels, called global interconnects, function like superhighways branching off into lower levels, or so-called local interconnects, that reach the individual transistors. See Fig. 1.4. The thickness of local interconnects must roughly equal the smallest feature size of the transistors, currently 32 nm, to avoid taking more space than the electronics themselves. As a result, nanowires are in use in current technology, so the conductivity degradation observed in them creates issues that we now summarize.

1.1.2   RC Delays

Following Plummer, Deal, and Griffin [60], we give a simple analysis of the inductance and capacitance of layers of interconnect. Let us first consider that the line resistance R of a wire is

$$R = \rho \frac{L}{A}, \tag{1.1}$$

where ρ is resistivity, L is wire length, and A is cross-sectional area. When transistor density doubles (which happens every two years by Moore's Law), typical transistor length scales (*i.e.* minimum feature size) only decrease by a factor of $\sqrt{2}$. So we already see that $L \to L/\sqrt{2}$ while the wire cross-section $A \to A/2$, so $R \to R\sqrt{2}$ every two years. We already have a problem and we have not even discussed conductivity degradation yet!

Making matters worse is the fact that the wires have inductance and capacitance, creating RC circuits that introduce resistivity-dependent delays [60]. The typical RC delay due to global interconnects [60] is $0.89RC \propto \rho$. Both increasing area and decreasing minimum feature size increase this delay, which competes with gate and other delays to limit performance (Figure 1.5). According to the 2007 International Technology Roadmap for Semiconductors (ITRS) [3]:

> [I]n the older 1.0 μm Al/SiO$_2$ technology generation the transistor delay
> was ~20 ps and the RC delay of a 1 mm line was ~1.0 ps, while in a
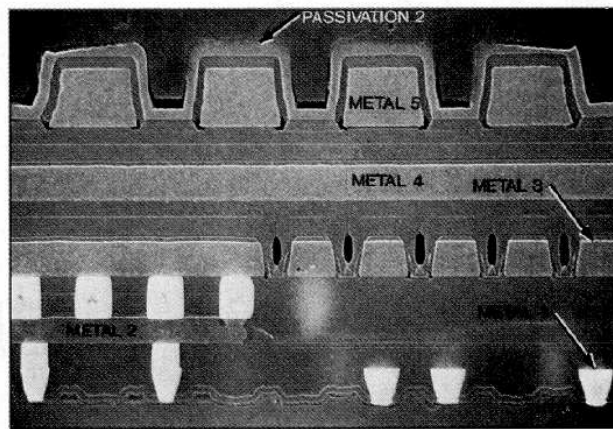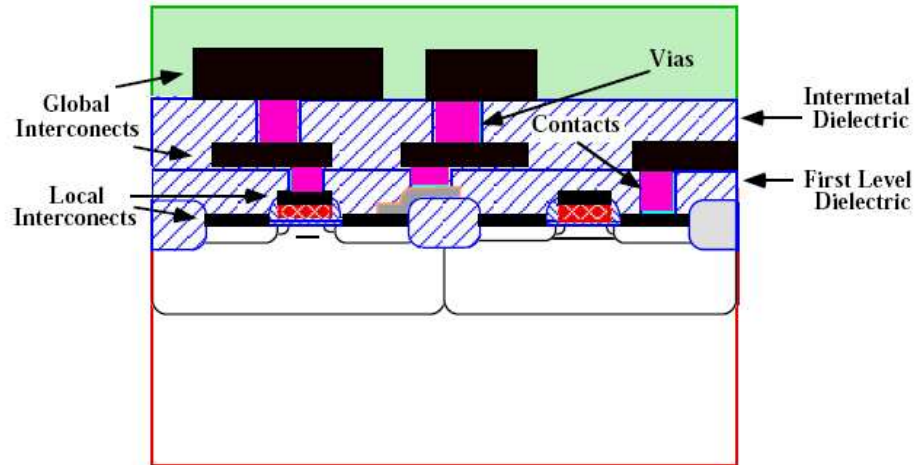
Figure 1.4: Schematic and photo of modern integrated circuit cross section. The highest layers of interconnect are like superhighways, branching down by **vias** to the bottom layers, or local interconnects, that must scale with transistor size. Both illustrations are from [60].
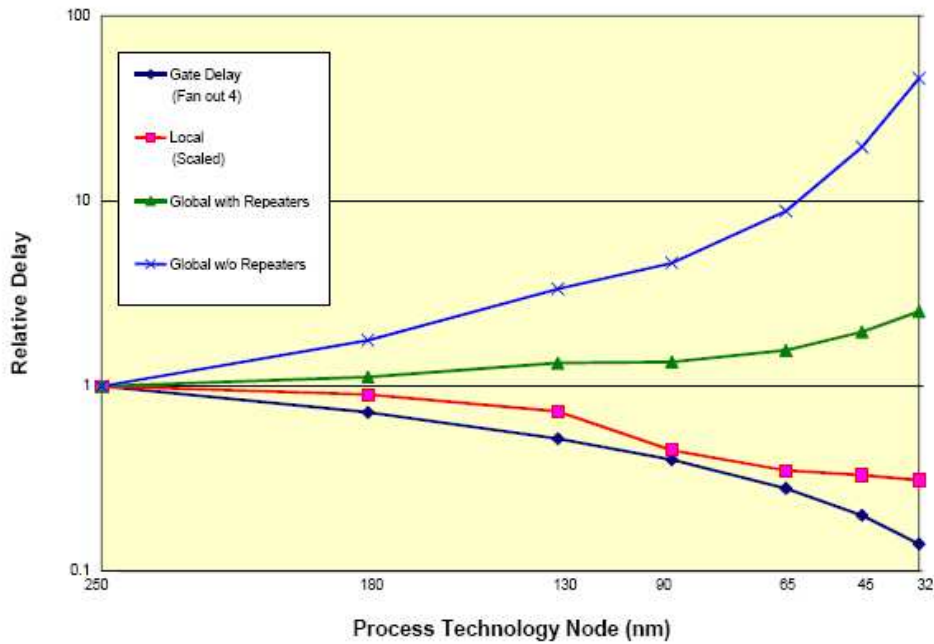
Figure 1.5: Interconnect delays, with gate delay for reference, for various technology generations. Figure is from [1].

projected 35 nm Cu/low-κ technology generation the transistor delay will be $\sim$1.0 ps, and the RC delay of a 1 mm line will be $\sim$250 ps.

1.1.3   Power Loss

Power consumption is currently a main focus of the semiconductor industry, as computers have reached a speed level that has proven generally satisfactory for consumers, and mobile devices like cellular phones and laptops are marketed based on battery life. Current generations of microprocessors waste a huge amount of power to heat, and must be cooled to keep this heat from degrading performance over both the short and long terms.

In this context, the power loss introduced by interconnects is very important, and is becoming one of the limiting factors in processor design. If the number of interconnections among transistors scales like t^2, where t is the number of transistors, then the power loss in the wires

$$P = I^2 R$$

where R is the wire resistance, increases greatly as the total wire length (even if slower than the total number of interconnections, $L \sim t^{1.5}$) increases *and* the resistivity gets worse.

According to the 2007 ITRS [3],

> [A]t 0.13μm approximately 51% of microprocessor power was consumed by interconnect, with a projection that without changes in design philosophy, in the next five years up to 80% of microprocessor power will be consumed by interconnect.

1.2 Thesis Overview: Causes of Degradation

The remainder of this chapter will introduce the focus of this dissertation, the causes of conductivity degradation.

The introduction of Cu wires for interconnect technology led to increased complexity and costs associated with depositing the wiring into integrated circuits. Cu atoms have a strong tendency to migrate into the low-dielectric-constant material that isolates each transistor, especially during subsequent process steps, which are done at elevated temperatures. As a result, a "liner layer" of another material is necessary that typically serves three purposes:

- Serve as a starting point for the deposition of interconnect metals onto dielectric

- Block migration of interconnect material into dielectric

- Adhere the interconnect to the dielectric
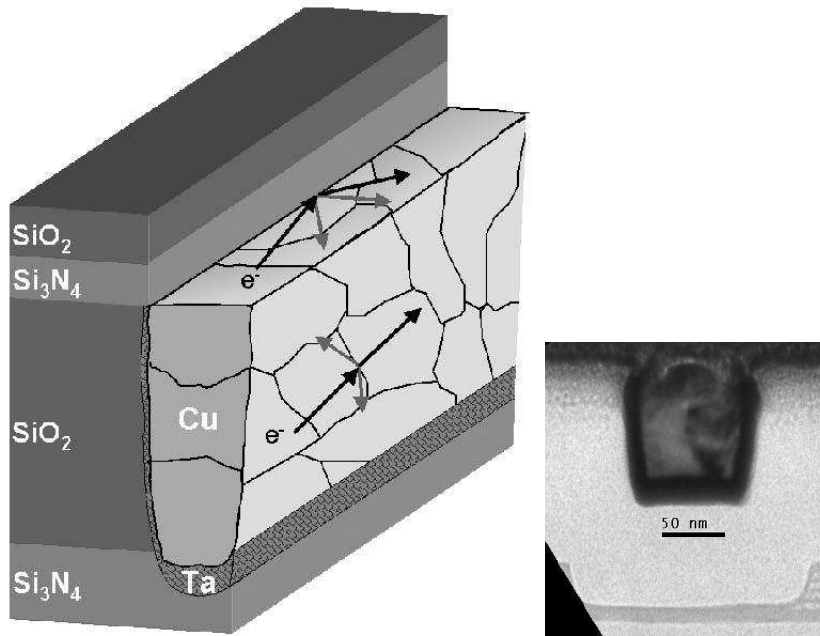
Figure 1.6: Schematic and photo of interconnect wire embedded in liner layer by a damascene method.

Additionally, modern interconnects are so small that they must be deposited atomically onto the substrate. Typically, interconnects are deposited by a "damascene" process which embeds liner layer and metal inside a groove in the dielectric, leaving them surrounded by dielectric on three sides with the fourth surface uncovered. Figure 1.3 illustrates this. Further metal or dielectric layers may be deposited on top of the fourth surface.

The figure also shows the three causes of conductivity degradation modeled in this work. In general, conductivity degradation comes from the **scattering** of current-carrying conduction electrons. The crooked lines shown within the Cu region represent **grain boundaries**, a scattering source explained in Section 1.2.2. In addition, the interface with the liner layer, a relatively poor conductor compared to Cu, is another source of scattering to be discussed below.

As a first step, we model both the interface with the liner layer and the uncovered

wire surface as interfaces with an insulator. Clearly, the uncovered surface really is an interface with insulator; for the other three surfaces, this represents a first approximation. Since the liner layer is a poor conductor, electrons are expected to transmit into the liner and return quickly into the Cu with randomized velocities. At an interface with an insulator, on the other hand, all electrons are reflected and remain in Cu. Our research plan is to start with this simplified model for all four sides of the Cu wire, and then refine our model by simulating transmission for the three interfaces with the liner layer.

1.2.1   Surface Scattering

1.2.2   Grain Boundary Scattering

In a crystalline material, a **grain boundary** is a boundary between crystallites, or regions of perfect crystal lattice, with different orientations. While the lowest energy configuration of a crystalline solid may be a perfect lattice structure[2], temperature effects will lead to various defects. Especially for extended defects like grain boundaries and dislocations, these are separated from the minimum-energy configuration by large energy barriers and can typically be removed only by annealing at high temperature.

Experimental evidence shows that grain size (or the distance between grain boundaries) in metals scales roughly with wire thickness [46, 4, 75], and that grain boundaries significantly affect conduction [6, 9, 18, 19, 28, 21, 44, 27, 48, 67, 68, 69, 81, 85]. These observations are incorporated into a simple semiclassical model of grain boundary conduction, the **Mayadas-Shatzkes (MS) model** [48] (see Chapter 2), which uses reflectivity R at each grain boundary as a single empirical parameter. However, previously to this work, no microscopic model of grain boundary conduction has been available to predict R or explain conduction.

---

[2]Actually, a "frozen phonon" may lower the energy for some anisotropic materials, in what is known as a Peierls distortion [45].

1.2.3 Interface Scattering

The liner layer is typically made of a material like Ta or TiN with small crystal grains [60]. This property impedes the migration of Cu atoms [60] but also makes the liner a poor conductor.

The interface between the Cu wire and the liner layer enveloping it is parallel to the direction of current flow. As a result, it is tempting to think of the wire-liner system as a pair of conductors (one with much higher conductivity than the other) in parallel. At fixed voltage, such a model predicts that the current through each conductor is independent of the presence of, and the number of opportunities to cross into, the other conductor.

However, this model is based on elementary circuit analysis, which assumes that independent (series) resistivity mechanisms add. But, as we will learn in Chapter 4, this assumption fails for bulk and surface scattering in a nanowire.

The surface scattering model sheds some light on the interface problem. When electrons move from Cu to liner, they are scattered with a much shorter mean free path than they would have if they remained in Cu. When they move from liner to Cu, their velocity is effectively random, since they will on average have had a recent scattering event. So the Cu/liner interface behaves much like a rough surface that randomizes electron velocity.

In order to improve over our surface scattering model, we need information on the reflection at the interface as a function of incident angle. This information can only come from microscopic considerations, whether theoretical or experimental.

1.2.4 Thesis Overview

Chapters 2 and 3 will continue to provide background, build the necessary theory, and introduce the concepts relevant to surface, grain boundary, and interface scattering. Chapters 4 – 6 will present the details and results of our calculations. Chapter 7 will

return to the overall picture and summarize what our results mean for interconnect technology.

Chapter 2

BACKGROUND

In this chapter, we review previous approaches to surface and grain boundary scattering in thin metal films and wires. In particular, we introduce the Fuchs-Sondheimer (FS) and Mayadas-Shatzkes (MS) semiclassical models of these phenomena. In addition to their quantitative validity, these models provide important physical insight into the nature of the problems. This Chapter can be seen as a summary of theory that will be useful in Chapter 4 and throughout this work. We will return to theory in Chapter 3, describing the transport formalism we use to address quantum transport through grain boundaries and interfaces.

2.1 *Literature Review*

Other approaches to surface roughness [78].

2.2 *Fuchs-Sondheimer Model of Surface Scattering*

The Fuchs-Sondheimer (FS) model [24, 73] treats transport semiclassically in thin rough metal films with both surface and bulk scattering. The fundamental assumption in this model is that a fraction p of electrons incident on the surface reflect specularly, and therefore continue with the same velocity v_z in the transport direction. The remainder of electrons scatter diffusely into a completely random state. Although this model fails to account for a dependence of the scattering probability p on the initial and final states, it can be tuned with p as a parameter to give the correct behavior. The FS model, with relatively robust assumptions, generally agrees with experimental observations.

There are other semiclassical models that introduce an angle-dependent scattering probability [70, 71], but these generally have complicated solutions. In order to derive the scattering probability from first principles, one must use a quantum mechanical treatment of the scattering event, as we do in Chapter 4.

The simplest case of the FS model to consider is $p = 0$, which was originally studied by Fuchs [24].

The FS model is usually given as

2.3   Mayadas-Shatzkes Model of Grain Boundary Scattering

The Mayadas-Shatzkes (MS) model [48, 49] is a semiclassical model of transport through a thin metal film punctuated by grain boundaries. Since the model is semiclassical, it does not differentiate between crystal grains on the two sides of the boundary, and in fact treats all crystalline regions in between boundaries via semiclassical transport with some mean free path λ_0 [48]. Moreover, it contains no microscopic treatment of grain boundaries and does not allow for scattering, only undeflected transmission or specular reflection.

The MS model assumes that all grain boundaries have "bamboo structure," meaning that they extend across the film, perpendicular to the film's surface (Figure **??**). So the transport direction z is normal to the grain boundaries [48].

The grain boundaries are represented by the potential

$$V(\vec{r}) = S\delta\left(\hat{z} \cdot \vec{r} - z_0\right),$$

where z_0 is the location of the grain boundary and S is the strength of scattering from a single boundary. Note that this potential depends only on the z-coordinate, so momentum is conserved in the x and y dimensions. Combined with energy conservation, this requires that

$$\vec{k} = (kx,\ ky,\ kz) \longrightarrow (kx,\ ky, \pm kz)$$

under scattering.

14
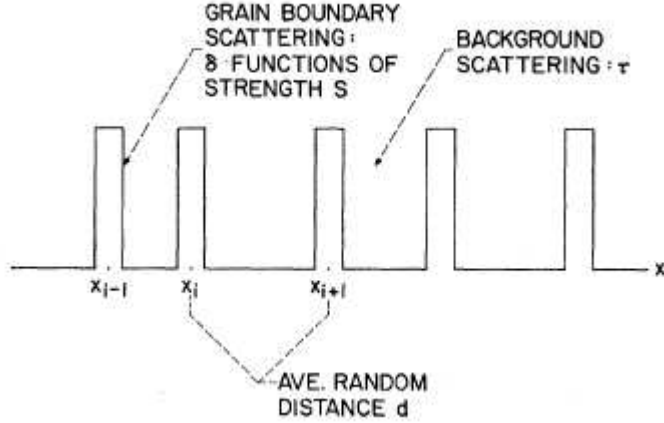
Figure 2.1: Distribution of grain boundaries and geometry of the Mayadas-Shatzkes (MS) model. Figure is taken from [48].

The MS model further assumes that grain boundary locations are distributed randomly by a Gaussian distribution with some mean separation d and standard deviation s (see Figure 2.1). The mean d is generally taken to be equal to the observed grain size D, and s is assumed large compared to the Fermi wavelength [49]. This leads to the most commonly-used form for conductivity in the MS model:

$$\frac{\sigma}{\sigma_0} = \frac{\rho_0}{\rho} = 3\left[\frac{1}{3} - \frac{1}{2}\alpha + \alpha^2 - \alpha^3 \ln(1 + 1/\alpha)\right], \qquad (2.1)$$

where

$$\alpha \equiv \frac{mS^2}{\hbar^3 dk_F} 2\tau \equiv \frac{\lambda_0}{D}\frac{R}{1-R}, \qquad (2.2)$$

σ_0, ρ_0, and λ_0 are the bulk conductivity, resistivity, and mean free path, and the boundary reflectivity R has been defined in terms of the delta-function strength S. R is equivalent to the probability of reflection for an incident electron wavefunction. Over most of the range of α, Eq. (2.1) can be approximated by [20]:

$$\frac{\rho}{\rho_0} \approx 1 + 1.39\alpha = 1 + 1.39\frac{\lambda_0}{D}\frac{R}{1-R}. \qquad (2.3)$$

It is common when applying the MS model to assume that $D \sim L$, that is, grain size is roughly equal to film thickness. This follows from observations in the original

MS papers [49, 47] that these two variables scale together. This was primarily based on observations of films deposited by evaporation, but still is roughly applicable for other deposition methods. While the damascene method can mitigate this to some degree by depositing larger-grained metals which are subsequently polished back to the desired nanoscale thickness, grain size still decreases with wire dimensions, so grain boundary scattering is potentially important in nanowires.

The Mayadas-Shatzkes model makes many assumptions, which we summarize here:

- Transport is semiclassical between grain boundaries.

- Grain boundaries are perpendicular to transport.

- Grain boundaries are translation-invariant along the boundary.

- Transmission at grain boundaries can be characterized by a single parameter R.

- All boundaries in a sample are identical (same R).

Some of these assumptions are clearly objectionable, and it seems likely that some may be wrong in a way that affects the final result. Let us consider the assumption of translation-invariant boundaries. In the presence of bulk scattering, velocities are randomized within a few mean free paths of the boundary, so the assumption of specular reflection or undeflected transmission may not matter, as long as R matches the average reflection probability. But if grain size is comparable to mean free path, or several boundaries are particularly close together, then the particular states transmitting through one boundary and incident on a second may affect overall transmission.

We simulate just such a system in Chapter 5, and we will further explore the validity of the MS model in Section 5.5. While the MS model may make unrealistic assumptions, it is currently the standard model used to extract boundary transmission information from experiments on conduction. The MS model remains one of the

few ways to bridge the gap between microscopic physics and macroscopic conduction experiments. Doing a first-principles simulation of two or more grain boundaries separated by a realistic grain size, together with the effects of bulk and surface scattering, is not currently practical. It is the aim of this thesis to narrow the gap between theory and observations with the computing power currently available.

Chapter 3

NON-EQUILIBRIUM ELECTRONIC TRANSPORT IN METALS

This chapter will discuss the theory of electronic transport through a conductor with a potential difference. It will review the Boltzmann Transport formalism and compare and contrast with Landauer Theory, a formulation particularly useful for mesoscopic systems. Landauer Theory is a special case of the Non-Equilibrium Green's Function (NEGF) Method, the calculational technique used in the present research to model grain boundary and interface scattering.

3.1 *Boltzmann Transport*

The Boltzmann Transport Equation (BTE) is a classical time evolution equation for a system of particles through phase space. It is notable because despite the key assumption of molecular chaos [30], it is very general and powerful.

Within the context of electronic transport, BTE is best suited to scattering-limited transport, when the phase coherence length of electrons is small, and therefore quantum mechanics makes negligible corrections. In a typical calculation, it is assumed that there is semi-classical propagation between scattering events; scattering must be calculated separately in quantum mechanics, and therefore outside of the confines of the Boltzmann formalism.

The Boltzmann Equation is closely related to the Liouville equation, and both express the conservation of particles in Hamiltonian flows. However, unlike the Liouville equation which is defined in configuration space, the BTE is defined in phase space. So it is possible for particle density to flow due to interactions and other forces.

This is expressed by the non-vanishing right hand side of the Boltzmann equation in steady state:

$$\frac{df_k}{dt} - \left(\frac{\partial f_k}{\partial t}\right)_{\text{Ext.Field}} - \left(\frac{\partial f_k}{\partial t}\right)_{\text{drift}} = \left(\frac{\partial f_k}{\partial t}\right)_{\text{collis}} = I. \tag{3.1}$$

Here the collision integral I defined by:

$$I \equiv \sum_{k'} (f_{k'} - f_k) \; W(k', k), \tag{3.2}$$

where W is a transition probability from k to k' due to interparticle interactions (typically collisions). The other partial derivatives are given by

$$\left(\frac{\partial f_k}{\partial t}\right)_{\text{Ext.Field}} = \frac{-e\vec{E}}{\hbar} \cdot \frac{\partial f_k}{\partial \vec{k}}, \; \left(\frac{\partial f_k}{\partial t}\right)_{\text{drift}} = -\vec{v_k} \cdot \frac{\partial f_k}{\partial \vec{r}}.$$

Typically, such calculations make use of the **relaxation time approximation (RTA)** [59, 64], which assumes that departures from equilibrium are small, and that the nonequilibrium part decays exponentially:

$$\left(\frac{\partial f_k}{\partial t}\right)_{\text{collis}} = I \approx \frac{-(f_k - f_k^0)}{\tau}, \tag{3.3}$$

where τ is a constant known as the **relaxation time**. Although our formalism for surface scattering in Chapter 4 will be based on a rigorous quantum mechanical formulation in NEGF by Meyerovich *et al* [52], the results are formally analogous to BTE, and τ in that chapter can be understood the same way as here. As we do in Chapter 4, one must typically compute the W and τ quantum mechanically, according to Fermi's Golden Rule. We will identify τ with the **momentum loss time**, which is computed from the transition rates W as the typical time it takes to lose momentum $\vec{k}$:

$$1/\tau = \sum_{\vec{k'}} W(\vec{k}, \vec{k'}) \; \frac{\vec{k} \cdot (\vec{k} - \vec{k'})}{k^2}. \tag{3.4}$$

Note that a grain boundary or interface between materials, unlike surface scattering, is not a small perturbation. Boundaries and interfaces have large spatial extents,

involve many dislocated and disordered atoms, and have different crystals on either side. In these systems, quantum effects are also important. Therefore, for our calculations in grain boundaries and interfaces, we will use Landauer Theory and NEGF to model conduction.

In steady state in the Boltzmann picture, the electron density reaches a uniform distribution:

$$\frac{\partial f_k}{\partial \vec{r}} = 0 = \left(\frac{\partial f_k}{\partial t}\right)_{\text{drift}},$$

and

$$\frac{df_k}{dt} = 0.$$

So mobility

$$\mu \equiv \frac{d\vec{v}}{d\vec{E}}$$

is given by $\mu = q\tau/m$, and current is limited by carrier velocity in response to scattering.

3.2   Landauer Theory

We discuss Landauer Theory before delving into the NEGF formalism because it is simpler, more physically transparent, and frequently adequate. In fact, Landauer Theory is equivalent to NEGF when electron-electron, electron-phonon, and similar dissipative interactions can be neglected [16].

To motivate the Landauer formalism (and as a concise way of understanding it), one may ask the question: If transport is not limited by scattering, is it limited at all? Traditionally, physicists have thought of transport as a balance between acceleration and scattering. If one removes scattering mechanisms (or considers conductors so short as to compare to a mean free path), one has "an ideal conductor" that responds to applied fields with "infinite current." Although the Boltzmann formalism can give a more realistic answer by tuning the carrier free path such that it is not longer than the total conductor length [15], the typical Boltzmann treatment, in which electrons
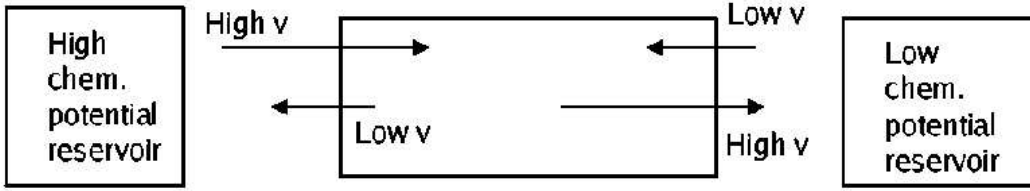
Figure 3.1: Schematic process illustrating Landauer Theory

are exposed to an electric field uniform throughout space, does not provide an obvious mechanism to limit conductivity.

Landauer theory, by contrast, makes explicit that current is limited by total potential difference. The Landauer picture is one of steady state, where electrons traveling through the conductor remain in equilibrium with their reservoir of origin (Fig. 3.1). As illustrated in Figure 3.1, net current flows due to an imbalance in the carrier velocities in the two reservoirs. Although the system is not in equilibrium, the carriers in the conductor reach a mean energy intermediate between that of the two reservoirs [17].

When the potential difference is sufficiently small, one can calculate the net current as a linear response to voltage in accordance with Ohm's Law. Here we do so following a discussion adapted from [16]. For a **ballistic** conductor (an ideal conductor limited only by voltage drop and the number of charge carrying modes), this follows simply from counting the current from each mode:

$$I = I^+ - I^- = \frac{2e}{L_z} \sum_{\vec{k}:\, k_z > 0} v_z(\vec{k}) \left\{ f_L\left(E(k)\right) - f_R\left(E(k)\right) \right\} \tag{3.5}$$

where I is a difference between forward- and reverse-moving currents I^+ and I^- in the $z-$direction, and L_x, L_y, and L_z are the dimensions of the conductor (which can

be taken $\to \infty$ if desired). Here the current from a single mode is

$$I_{z,k} = j_z L_x L_y = \rho \, v_z L_x L_y = \frac{2e v_z}{L_z},$$

with a factor of 2 for spin. We have used the reflection symmetry of the Fermi surface to write

$$v_z(k_x, k_y, -k_z) = -v_z(k_x, k_y, k_z).$$

Then the only difference between I^+ and I^- is a relative minus sign and the equilibrium electron populations f_L and f_R in the originating reservoirs. Since the electrons remain in equilibrium with their electrodes of origin, these are just Fermi distributions centered at E_F and $E_F + eV$.

We assume $eV \ll E_F$ for linear response. It is helpful but not necessary to take $kT \ll eV$ so we do not have to consider smearing of Fermi levels. We convert the discrete summation to integration using $d^3k = (2\pi)^3/L_x L_y L_z$:

$$I = \frac{2e L_x L_y}{(2\pi)^3} \int_{k_z > 0} d^3k \, v_z(\vec{k}) \left\{ f_L\left(E(k)\right) - f_R\left(E(k)\right) \right\},$$

and break the integration into a portion $d^2 k_{||}$ tangent to the constant energy surface and a portion $dk_\perp \propto dE$ in the direction of the group velocity

$$\vec{v}(\vec{k}) = \frac{1}{\hbar} \vec{\nabla}_k E = \frac{dE}{\hbar dk_\perp} \hat{k}_\perp.$$

We next note that

$$v_z \, dk_\perp = \frac{1}{\hbar} \frac{dE}{dk_\perp} \hat{k}_\perp \cdot \hat{z} \, dk_\perp = \frac{dE}{\hbar} \, \hat{k}_\perp \cdot \hat{z},$$

so that

$$I = \frac{2e L_x L_y}{h(2\pi)^2} \int dE \left\{ f_L\left(E\right) - f_R\left(E\right) \right\} \int d^2 k_{||} (\hat{k}_\perp \cdot \hat{z}) \equiv \frac{2e}{h} \int_{E_F}^{E_F + eV} dE \, M\left(E\right).$$

Here we have used the low temperature limit of f_L and f_R and have defined

$$M(E) \equiv \frac{A}{(2\pi)^2} \int d^2 k_{||} \, (\hat{k}_\perp \cdot \hat{z}) = \frac{A}{(2\pi)^2} \int d^2 k,$$

22

with $A = L_x L_y$. In the last equality, we use Gauss' Theorem to write $M(E)$ as an integral over a cross section of the constant-energy surface. So $M(E)$ is equal to the number of forward-moving modes with cutoff energy $E_C < E$ [16]. For linear response[1], we must take

$$eV \ll \frac{M(E)}{dM/dE},$$

so that $M(E) \approx M(E_F)$; in other words, both reservoirs have the same conduction electron density. Then:

$$I_0 = \frac{2e^2}{h} \, M(E_F) \, V \equiv GV, \tag{3.6}$$

where we have introduced the symbol I_0 to represent ballistic current. We find that conductance per unit cross section G/A in a ballistic conductor is "quantized" in units of $2e^2/h = 77.5 \, \mu\mathrm{S}$ [16, 17]! This is due to the finite number of charge carriers, or equivalently, the finite number of modes inside the Fermi surface of a conductor of finite size.

To add elastic scattering to the picture, we insert a transmission probability for each mode $\vec{k}$

$$T(\vec{k}) = \sum_{\vec{k}' \, : \, k_z' > 0} P_{\vec{k} \to \vec{k}'} = \sum_{\vec{k}' \, : \, k_z' > 0} \left| \left\langle \vec{k} \, |S| \, \vec{k}' \right\rangle \right|^2, \tag{3.7}$$

where S is the usual scattering S matrix as in Refs. [66, 50]. This approach is well suited to static scatterers like impurities and grain boundaries, where carriers either reflect or continue with the same energy. Note that in a steady state (over length scales smaller than a mean free path), net current is the same for all forward moving modes because the density of states at a given (k_x, k_y) and $|v_z|$ are inversely proportional on an energy surface. We saw this already in the derivation of Eq. (3.6). For this reason, only T in (3.7), and not v_z in the final state, matters for the current. Over larger length scales, bulk scattering would keep the small-v_z states from contributing as much to current.

---

[1]In this work, we are interested only in the lowest order response to an applied field. But calculations for finite bias can also be done by keeping the integrals over E.

By the same reasoning, we can replace $T(\vec{k})$ by its average $\bar{T}/M$, where

$$\bar{T} \equiv \sum_{\vec{k}} T\left(\vec{k}\right) \tag{3.8}$$

is known as the **transmission function** [16]. The result for the current is

$$I = \frac{\bar{T}(E_F)}{M(E_F)} I_0 = \frac{2e^2}{h} \bar{T} V. \tag{3.9}$$

Much of the rest of this thesis will be devoted to calculating $T(\vec{k})$ and $\bar{T}$ for grain boundaries and interfaces. These results can be made equivalent to the Boltzmann Formalism by tuning $\bar{T}$ [15].

Formally, the Landauer picture is valid when dissipative interactions, like phonon and electron-electron scattering, that would break the equilibrium between the electrons and their originating electrodes are negligible. Landauer theory can be extended to treat electron-electron interactions at a mean field level by considering electrons as quasiparticles; but it does not generally incorporate fluctuations about this mean or phonon scattering[2]. The strength of the Landauer formalism is its intuitive transparency in situations to which Boltzmann Transport is poorly suited, such as mesoscopic systems where length scales of transport are small compared to the phase coherence length and mean free path.

3.3   *Non-Equilibrium Green's Functions*

The NEGF formalism, also known as the Keldysh formalism, is valid when quantum correlations are important, but when dissipative interactions are also present [16]. It can be thought of as an extension of Landauer Theory to cases with dynamical scattering, or of Boltzmann Transport to cases when propagation is quantum mechanical. To put matters even more simply, Landauer Theory becomes NEGF when one calculates transmission probabilities T in terms of Green's functions and self-energies.

---

[2]See, however, [31].

In this thesis, we use NEGF to calculate the transmission probabilities (3.7) across grain boundaries and interfaces between materials. Clearly, such systems, which have disorder on atomic length scales, require a quantum treatment. However, far from the interface or boundary, such systems have regular crystals and scattering is dominated by phonons, which as usual can be treated as perturbations to semiclassical transport[3]. Therefore, we do not need to consider the regions far away from the boundary or interface. Nor do we simulate phonons in the boundary, although any synergistic effects between phonons and the boundary are likely accounted for by lattice disorder [63]. Our treatment is a fully quantum-mechanical calculation from first principles in Density Functional Theory [38, 37] (DFT; see Section 3.4 for a brief overview), and is non-perturbative.

3.3.1   Overview

Essentially, NEGF or the Keldysh formalism is diagrammatic perturbation theory applied to the meta-stable electronic states that can interact with phonons, other electrons, and other impurities, and hence can decay. A recommended introduction to NEGF is given in [16].

NEGF can be best understood by considering corrections to the free-electron gas model, also known as the Sommerfeld Model, of normal metals [8]. The Sommerfeld Model works surprisingly well, considering the strength of the Coulomb interactions between electrons [8]. There are many approaches to correcting this model, including Hartree-Fock Theory and Fermi Liquid Theory. Although these methods approach interactions differently, most of them treat interactions at a **mean-field level** by representing the electronic ground state by single-particle states exposed to a mean

---

[3]However, as we will see in Section 5.5, our research indicates flaws in the Mayadas-Shatzkes model, which assumes that transport between grain boundaries is semi-classical. This could be because boundaries are close enough to interact, or it could be due to other assumptions in MS, such as that transmitted electrons are undeflected by the boundary or that R is independent of incident angle.

field potential from the other electrons [8]. Although electron-electron interactions can be strong, the fluctuations about this mean-field level are small. So the Sommerfeld Model is very nearly valid, provided we remember that the free-gas particles are actually not electrons, but fluctuations called **quasiparticles** about the mean field.

Fermi Liquid Theory makes explicit that the "electrons" in the free-gas model are actually **quasiparticles**, or perturbations about the ground state of the system. In a metal, a quasiparticle is simply an interacting electron excited slightly above the Fermi surface, together with the cloud of electrons that screen the excited electron's charge. Clearly, any quasiparticle excited above the Fermi surface can decay into available states lower in energy. The mechanism that makes this decay possible – and therefore makes a quasiparticle not an eigenstate of the full Hamiltonian – are interactions with phonons, lattice impurities, and other electrons through fluctuations in the mean electron density.

Before we move on to learning NEGF, consider that in principle, the metal as a whole has a Hamiltonian with a complete set of energy eigenstates. A key concept is that we do not *need* to know the eigenstates of the full conductor Hamiltonian in order to study transport. Even if the conductor were isolated from the rest of the world, finding such eigenstates would be very difficult, but is unnecessary. The reason is that interactions[4] are small and can be treated perturbatively. If interactions were extremely strong, one would need to be prepared to treat the whole system of interacting particles (the lattice as well as the electrons) if one wanted to say anything about the physics of conduction. Because interactions are perturbative, the simpler description in terms of quasiparticles is very accurate. The real conductor contains conducting quasiparticles with long lifetimes.

Throughout this thesis, we can use the terms "quasiparticle" and "electron" interchangeably, provided we remember that a quasiparticle is an electron together with

---

[4]The term *interactions* is used generically to refer to fluctuations about the mean electronic field as well as to interactions with phonons and defects.

the average cloud of charge density that follows it around due to electron-electron interactions.

3.3.2 Theory

The fact that quasiparticles are not exact eigenstates, but weakly interacting particles, leads to two effects:

- A shift in the energy levels of quasiparticles due to the energy of interaction.

- A broadening of the quasiparticle energies due to the fact that the eigenstates are no longer exact. This is equivalent to a finite lifetime.

Both of these effects can be treated by adding a **self-energy**

$$\Sigma = \mathrm{Re}\{\Sigma\} + i\,\Gamma \tag{3.10}$$

to the quasiparticle energy [5, 16].

The (retarded) **Green's function** of the system is defined as

$$G(E) \equiv \lim_{\delta \to 0^+} [(E + i\delta)1 - H]^{-1} \tag{3.11}$$

and is a propagator for the full Hamiltonian [66, 50, 26, 16] containing full information about the system's dynamics. When we refer to the Green's function G it should be understood to mean the retarded one, and we will use $G^\dagger$ to refer to the advanced Green's function. We will also not explicitly write $i\delta$, but it should be understood to be present unless we explicitly specify otherwise.

Let us assume there is some unperturbed (quasiparticle) Hamiltonian H_0 subject to some perturbations (interactions or leads). Then

$$G(E) = [E - H_0 + \Sigma]^{-1},$$

where Σ is the self-energy of the perturbation [16]. This equation means that we can continue to treat the system from a single-particle point of view and simply

correct H_0 by including the self-energy Σ. The imaginary part Γ of Σ gives rise to finite quasiparticle lifetime (broadening of levels), and the real part to shifts of the unperturbed energy levels. Computing the self-energy for interactions [16] is in general a complex problem, but here we will discuss only self-energies for electrodes (see Sec. 3.3.4).

3.3.3 Fisher-Lee Relation

The **Fisher-Lee relation** [23, 16] is a relationship between the scattering S matrix and the Green's function of the system. That such a relation exists is completely reasonable since the S matrix is often defined as the propagation over the limit of very long times of incoming asymptotic states into outgoing ones, and the Green's function is a propagator for the full Hamiltonian [66, 50, 26, 16].

The Fisher-Lee relation applies to problems like ours with a localized scattering source and well-defined free states far from the scatterer. In scattering theory, a localized scatterer generally means a small target particle to be treated in spherical coordinates, but for the conduction problem we work in planar geometry with transport direction z. Following Datta [16], we use a separate coordinate system in each lead with origin at $z \to \pm\infty$, so that we do not have to consider the e^{ikz}-dependence[5] of G. Then the Fisher-Lee relation follows immediately from writing down the Green's function G as a sum over propagating modes times the amplitude (given by the S matrix) to be in the mode:

$$G(\rho, 0; \rho', 0) = - \sum_{m \in L,\, n \in R} \frac{i\, S_{nm}}{\hbar \sqrt{v_m v_n}}\, \psi_m(\rho)\, \chi_n^*(\rho') \tag{3.12}$$

using cylindrical coordinates $\rho \equiv (x, y)$ and the two origins $z = 0$ and $z' = 0$ deep inside the left and right electrodes, far from the scatterer.

---

[5]Equivalently, where one sees $G(\rho, 0; \rho', 0)$, one can substitute the Green's function $G(\rho, z; \rho', z')$ divided by its z- and z'-dependence.

Here ψ_m and χ_n are a basis of transverse modes for the left and right electrodes and v_m and v_n are their group velocities in the z direction. We assume the eigenfunctions of the leads are $\psi_m(\rho)\, e^{ikz}$ or have a similar Bloch-like z-dependence. Then ψ and χ obey orthogonality relations in the transverse dimensions:

$$\int \psi_m^*(\rho)\, \psi_n(\rho)\, d^2\rho \;=\; \delta_{nm}.$$

The Fisher-Lee relation follows immediately:

$$S_{nm} = i\hbar\sqrt{v_n v_m} \int \chi_n(\rho')\, G\left(\rho, 0; \rho', 0\right)\, \psi_m^*(\rho)\, d^2\rho\, d^2\rho' \qquad (3.13)$$

with $m \in L$, $n \in R$.

With the Fisher-Lee relation, we see that we can calculate all our desired transmission probabilities, Eq. (3.7), in terms of the Green's function G for propagation across the scattering region. As we discussed above, we can find the Green's function for the full system by including the self-energies of the various interactions. We will not explicitly describe the calculation of interaction self-energies because we do not treat these in the present work (for an overview, see [16] and references therein). However, lead self-energies are central to our method.

3.3.4   Couplings to Leads

Phonons and electron-electron interactions cannot be "turned off." But lead self-energies provide a nice illustration of NEGF concepts, because the isolated conductor without leads is a quantum system with exact, quantized energies [17, 16]. Then the coupling of this conductor to electrodes broadens and shifts the energy levels [17].

NEGF treats this sytem in a way very analogous to a statistical mechanics treatment of an open system. In statistical mechanics, switching from an isolated system to one in contact with a particle bath requires a switch from the system internal energy U to the thermodynamic potential, $U - \mu N$ [64, 30]. When we connect our

conductor to its leads, we switch from the Hamiltonian H_c for a quasiparticle in the isolated conductor to a modified Hamiltonian $H_c + \Sigma$.

To make this explicit, consider the Hamiltonian

$$H = \begin{pmatrix} H_e & \tau \\ \tau^\dagger & H_c \end{pmatrix}$$

of the conductor H_c coupled by τ to a periodic semi-infinite electrode with Hamiltonian H_e. We wish to cut off part of this infinite chain (see Figure 3.2) in a way that does not cause reflection. Then

$$G(E) = \frac{1}{E - H} = \begin{pmatrix} G_e & -g_e\tau G_c \\ -g_c\tau^\dagger G_e & G_c \end{pmatrix} \tag{3.14}$$

with

$$g_e \equiv (E - H_e)^{-1}, \; g_c \equiv (E - H_c)^{-1}$$

the Green's functions of the *isolated* electrodes and conductor, and

$$G_e \equiv (E - H_e - \Sigma_e)^{-1}, \; G_c \equiv (E - H_c - \Sigma_c)^{-1}$$

the Green's functions for the open interacting electrodes and conductor.

Note that, as promised in Sec. 3.3.2, the conductor Green's function G_c is modified from its isolated counterpart g_c only by a lead self-energy

$$\Sigma_c \equiv \tau^\dagger g_e \tau. \tag{3.15}$$

Likewise, the electrode Green's function G_e is modified from g_e by

$$\Sigma_e \equiv \tau g_c \tau^\dagger.$$

Eq. (3.14) can be verified by direct multiplication.

Physically, the anti-Hermitian part Γ of Σ (Eq. (3.10)) represents particle "annhilation" and "creation" due to inflow and outflow at the contacts between the conductor
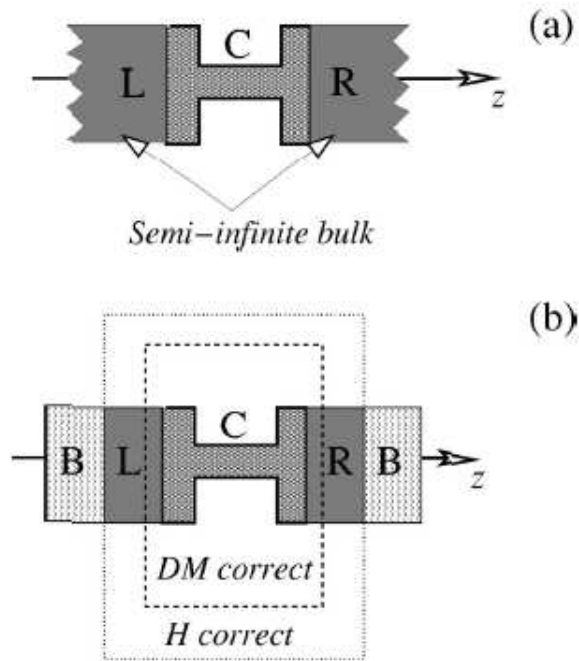
Figure 3.2: Including a finite part of the infinite electrodes in the simulated cell. The rest of the electrodes can be included by a lead self-energy. This figure is taken from [10].

and electrodes. Since we are only interested in the Green's function for propagation from the left electrode across the scattering region (generally the self-energy also includes a contribution from the right electrode, $\Sigma = \Sigma_L + \Sigma_R$), we can work only with G_c. So we can take into account the effect of the lead completely by including it as a self-energy.

3.3.5   Calculating Conductance

The total current is given by Eq. (3.9), with the transmission $\bar{T}$ defined by (see Eqs. (3.7) and (3.8))

$$\bar{T} = \sum_{m\in L,\, n\in R} |S_{m,n}|^2, \tag{3.16}$$

where m and n are the modes in the left and right leads, respectively [16]. It follows [16, 10] from substituting the Fisher-Lee relation (3.13) into Eq. (3.16) that

$$\bar{T} = \mathrm{Tr}\left[\Gamma_L\, G^\dagger\, \Gamma_R\, G\right], \tag{3.17}$$

with $\Gamma_{L,R} = \mathrm{Im}\,\{\Sigma_{L,R}\}$ the anti-Hermitian part of the lead self energies from Eq. (3.15). Based on this, we make the definition [10]

$$t \equiv \Gamma_R^{1/2}\, G\, \Gamma_L^{1/2} \tag{3.18}$$

of the (left-to-right) transfer matrix, so that

$$\bar{T} = \mathrm{Tr}\, t^\dagger t. \tag{3.19}$$

Note that the left and right leads generally can have different bases U_L and U_R of (asymptotic) eigenstates [10]. So

$$t = U_R\, \mathrm{diag}\{|\tau_n|\}\, U_L^\dagger$$

is the *left-to-right* portion of the scattering S matrix, and

$$t^\dagger = U_L\, \mathrm{diag}\{|\tau_n|\}\, U_R^\dagger$$

is the right-to-left one. The full S matrix [23]

$$S = \begin{pmatrix} r_L & t^\dagger \\ t & r_R \end{pmatrix}$$

is unitary as usual, giving relationships like $r_L^\dagger r_L + t^\dagger t = 1$. If the system obeys time-reversal symmetry, then

$$\langle -\vec{k} \,|\, t \,|-\vec{k'}\rangle \;=\; \langle \vec{k} \,|\, t^\dagger \,|\, \vec{k'}\rangle, \tag{3.20}$$

where $\vec{k}$ and $\vec{k'}$ are asymptotic states in the right and left electrodes. But even without this symmetry, the properties of the trace guarantee that

$$\bar{T} = \mathrm{Tr}\,\{t^\dagger t\} = \mathrm{Tr}\,\{t\,t^\dagger\} = \sum_n |\tau_n|^2. \tag{3.21}$$

In other words, for a system with two leads, the transmission function is equal in either direction [16].

3.3.6 NEGF Calculations in this Work

In this work, all NEGF calculations (Chapters 5 and 6) have been done using Atomistix, a commercial NEGF code. Atomistix is described in Ref. [10] and references therein.

As described there, Atomistix simulations proceed by calculating the Green's functions g_e for the isolated semi-infinite leads (regions "B" in Fig. 3.2; represented by an atomic structure with periodic boundary conditions), then including these as a self-energy in the main calculation of G_c. The central or interacting region G_c is represented, as in Fig. 3.2, as an atomic structure in a cell with periodic boundary conditions transverse to the transport direction.

Atomistix then calculates the transmission amplitude matrix t, as in Eq. (3.18), from the Green's function $G_c(E)$ for propagation from one lead to the other.

The entire $G_c(E)$ calculation is done on a region called the **supercell** (shown in the box labeled "H correct" in Fig. 3.2), which consists of the central region and one

periodic cell each of the left and right electrodes. In Atomistix, the central region must terminate in layers that match the structure of the electrodes, so that the electrodes and central region can be joined unambiguously. The entire supercell has periodic boundary conditions transverse to the transport direction.

Atomistix uses Density Functional Theory (DFT; described in the next section) to find self-consistent effective electronic potentials in response to the atomic structure and the lead self-energies. Atomistix is based on TranSIESTA [10], an extension of the static DFT code SIESTA [72] to handle transport calculations using lead self-energies.

3.4   Density Functional Theory

Within the context of NEGF, our calculations use **Density Functional Theory** (DFT) to treat the many-body problem of conducting electrons. We give only a very brief overview here, as DFT is a well-known topic and many good reviews exist. Some recommended starting points are Refs. [38, 37].

Density Functional Theory is a formally exact approach to calculating the ground state of a many-electron system. It is similar in spirit to Thomas-Fermi Theory and Hartree-Fock Theory, except that it includes both exchange effects and electron-electron Coulomb interactions exactly [38]. Unlike other exact approaches, it focuses on the electron probability density n as the fundamental variable of the ground state.

The Kohn-Sham [38] formulation of DFT states that the ground state energy E and density n of a quantum system of N interacting particles are given by

$$E = \sum_{j}^{N} \epsilon_j + E_{XC}\left[n\right] - \int V_{XC}(r)\, n(r) d^3 r - \frac{1}{2} \int \frac{n(r)\, n(r')}{|r - r'|}\, d^3 r\, d^3 r' \qquad (3.22)$$

and

$$n(r) = \sum_{j}^{N} |\phi_j(r)|^2 \qquad (3.23)$$

where the ϕ_j are like independent particle states. That is, these states obey a single

particle Schrodinger equation called the **Kohn-Sham (KS) equation**:

$$\left(-\frac{\hbar^2 \nabla^2}{2m} + V_{eff}\right)\phi_j \;=\; \epsilon_j\,\phi_j\,. \tag{3.24}$$

But note that the definitions of V_{XC}, E_{XC}, and V_{eff} are recursive:

$$V_{eff}(r) \equiv V(r) + \int \frac{n(r')}{|r-r'|}d^3r + V_{XC}(r),$$

$$V_{XC}(r) \equiv \frac{\delta}{\delta n(r)}E_{XC},$$

$$E_{XC}[n(r)] \equiv F[n(r)] - T_s[n(r)] - \frac{1}{2}\int \frac{n(r')n(r)}{|r-r'|}d^3r,$$

where $F[n(r)]$ is the minimum value of kinetic plus interaction energy, $T+U$, for any electronic wavefunction ψ, subject to the constraint that ψ gives rise to density n. $T_s[n(r)]$ is the kinetic energy of a set of *noninteracting* electrons with density n [38]. We give these recursive definitions here primarily to point out that solving the KS equation must generally be done self-consistently, by iteration.

One should also note that DFT emphasizes that knowledge of the ground-state density n, in addition to the fact that the ground state always obeys the the Rayleigh-Ritz Minimum Principle

$$E_{gs} = \min_{\Psi}\langle H \rangle = \min_{\Psi} \frac{\langle \Psi\,|H|\,\Psi \rangle}{\langle \Psi|\Psi \rangle},$$

is sufficient to calculate the external potential V and therefore the full Hamiltonian and all expectation values of the system [12]. Hence, DFT makes n the central variable of (ground-state) quantum mechanics, a directly observable quantity that in principle contains complete information about the system.

However, in practice, solving the KS equations for n (or using n to compute other observables) is impossible without making some approximations [38, 37]. In addition to choosing a form for $E_{XC}[n]$, which is a huge topic in itself [38, 37], one must also truncate the self-consistent search for n. In particular, our calculations use DFT only at the mean field level [10]. In other words, while DFT in principle can account for

the electron-electron interactions exactly, in practice we treat the KS eigenstates as noninteracting quasiparticle states when calculating quantities like electronic current. Thus DFT becomes a mean-field theory like Hartree-Fock theory, where electronic states are single-particle KS states solved in a self-consistent mean Coulomb field (with exchange effects) of the other electrons.

Chapter 4

SURFACE SCATTERING

In this chapter, we investigate the detailed dependence of conductivity on surface roughness profile and analyze the resulting technological impact.

4.1   Theoretical background

The first quantitative treatments of surface and size effects in thin films or wires were the semiclassical methods of Fuchs [24] and Sondheimer [73]. These approaches assume a ratio p of carrier collisions with the surface reflect specularly, while $1 - p$ scatter diffusely. Such theories can be fit to experiment with p as a free parameter, but do not provide insight into how to improve conductivity.

More recently, surface roughness scattering has raised the attention of researchers in industry [13, 33, 34], and quantum mechanical approaches to surface scattering calculations have been proposed. The two primary approaches include the Kubo linear response theory of Tešanović *et al.* [77] and Trivedi and Ashcroft [80], and the diagrammatic Keldysh formalism of Meyerovich and collaborators [52, 53, 51]. Here we follow the approach of Meyerovich *et al.*, which is readily applied to arbitrary surface roughness profiles. We calculate the contribution of each spatial frequency of surface roughness and convolve with roughness data extracted from experiments to gain insight into the nature of surface roughness scattering.

In our conductivity calculations, we consider a thin film because it reproduces the major qualitative results of a wire (and matches quantitatively when Eq. (4.11) below holds), while avoiding strong localization and other effects that make 1D systems problematic to deal with theoretically [51, 42]. For the technologically important 10-

100 nm scale, wire conductivity can be accurately estimated by combining effects of scattering from sidewalls to that from top and bottom surfaces.

In a thin film of thickness L, boundary conditions at the surfaces lead to a density of states quantized in the transverse direction. As a result, the conduction band, described as the set of states at the Fermi energy, is broken into **subbands** with continuous parallel and quantized transverse components of the Bloch wavevector (Figure 4.1). Conduction states are then described by a subband index j and a 2D wavevector $\vec{k_j}$, subject to the constraint that the total energy is equal to the Fermi energy:

$$E = \frac{\hbar^2}{2m^*} \left[\left(\frac{\pi j}{L} \right)^2 + k_j^2 \right] = E_F \tag{4.1}$$

(We treat the Fermi surface as effectively spherical, which is particularly appropriate for the best conducting metals, Ag, Cu, and Au). Even in a perfectly smooth film, this quantization leads to thickness-dependent conductivity, and to the quantum size effect (QSE), caused by the quantized dependence of the density of states on thickness [80] which is significant for very thin films (<5nm).

Theoretical approaches to rough surfaces [77, 52] employ a (non-unitary) transformation to map the film with position-dependent thickness

$$L + h_1(x, y) + h_2(x, y),$$

where h_1 and h_2 are the deviations in the top and bottom surfaces from their average level, into a flat film with bulk (non-Hermitian) perturbations. Here we assume that both random functions h_1 and h_2 have the same correlation function,

$$\zeta(\vec{x}) \equiv \int h(\vec{x'}) \, h(\vec{x'} + \vec{x}) \, d^2 x'. \tag{4.2}$$

The scattering then depends on the **power spectral density** (PSD) of the roughness, defined as the Fourier transformed surface height correlation function

$$\zeta(\vec{k}) = \int e^{i\vec{k}\cdot\vec{x}} \, \zeta(\vec{x}) \, d^2 x \tag{4.3}$$
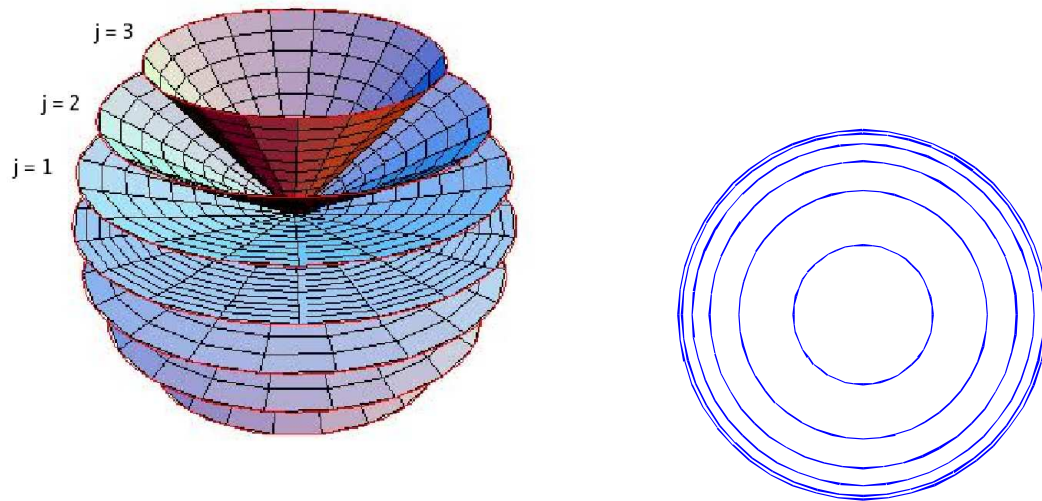
Figure 4.1: Quantization of electronic states into subbands in a thin film. Depicted schematically is a constant-energy surface in k-space (an actual wave function would be a standing wave, not propagating, in the vertical dimension) and a top view of this surface. Only discrete values of $k_z = \frac{\pi j}{L}$ are allowed in the vertical dimension, which represents the dimension in which the film is thin. Note that higher-j subbands have *smaller* in-plane k_j, and that the spacing between these is larger than for the lower-j subbands. This fact will be important in understanding the importance of quantization for low-spatial-frequency roughness.

We assume that the correlation function and PSD are isotropic, $\zeta(\vec{k}) = \zeta(|\vec{k}|)$.

In [52, 51], a general isotropic 2D roughness power spectrum $\zeta(|\vec{k}|)$ is treated with diagrammatic perturbation theory. By Fermi's Golden Rule, the presence of roughness at spatial frequency k allows a transition from initial state $\vec{k_i}$ to final state $\vec{k_f}$ if

$$k = |\vec{k_i} - \vec{k_f}| = \sqrt{k_i^2 + k_f^2 - 2k_i k_f \cos \chi},$$

where χ is the angle between initial and final carrier momentum. So the PSD determines both the intra- and interband transition rates, and hence a momentum loss rate *matrix* [51]:

$$W_{jj'}(\chi) = \frac{2\hbar}{(m^* L)^2} \left(\frac{\pi j}{L}\right)^2 \left(\frac{\pi j'}{L}\right)^2 \zeta(k_j, k_{j'}, \chi), \tag{4.4}$$

$$(\tau_s)_{jj'}^{-1} = \frac{m^*}{2} \sum_{j''} \left[\delta_{jj'} W_{jj''}^{(0)} - \delta_{j'j''} W_{jj'}^{(1)} \right]. \tag{4.5}$$

Here $\hbar k_j$ is the in-plane momentum satisfying (4.1) for subband j, j and j' are the initial and final subbands, $\zeta(k_j, k_{j'}, \chi) = \zeta(\sqrt{k_j^2 + k_{j'}^2 - 2k_j k_{j'} \cos \chi})$, and superscripts denote (2D) angular harmonics:

$$W_{jj'}^{(n)} \equiv \frac{1}{\pi} \int_0^{2\pi} d\chi \, W_{jj'}(\chi) \cos(n\chi). \tag{4.6}$$

The difference of angular harmonics in Eq. (4.5) can be thought of as analogous to the projection of momentum loss in the transmission direction in Eq. (3.4).

In the surface roughness-limited case (negligible bulk scattering), conductivity is given by

$$\sigma_s = 1/\rho_s = \frac{\tau_s \, n e^2}{m^*} = \frac{e^2}{2\pi \, m^* L} \sum_{jj'} k_j \, \tau_{jj'} \, k_{j'}, \tag{4.7}$$

where ρ_s is resistivity, the scalar τ_s is the overall surface-limited relaxation or mean free time, $n = k_F^3/3\pi^2$ is carrier density, and $1/\tau_s \propto \rho_s$ is the overall surface momentum loss rate. Note that our definition differs from [51] by an extra factor of $3/2\pi L$ because we use the usual 3D conductivity, as in [80].

To combine bulk and surface scattering, we extend the method in [80], adding momentum loss rates within subbands, to the case with interband transitions by adding matrices: $\tau^{-1} = \tau_b^{-1} + \tau_s^{-1}$. Since the primary bulk scattering mechanism at room temperature, acoustic phonons, is nearly isotropic [79], we use

$$(\tau_b)_{jj'}^{-1} = \frac{v_F}{\lambda_b}\delta_{jj'},$$

with $v_F = 1.6 \times 10^8$ cm/s the Fermi velocity and $\lambda_b = 39$ nm the bulk mean free path for copper.

4.2 Results

Adding matrices produces very different results from adding the scalars $1/\tau \propto \rho$. Matthiessen's rule, which states that $\rho_T = \rho_1 + \rho_2$ for independent (series) resistivity mechanisms, breaks down in thin films when combining bulk and surface scattering [76, 53, 80, 56] (Fig. 4.2 below). This breakdown can be understood because, absent bulk scattering, conductivity is dominated by carriers with momentum nearly parallel to the surface (low j) which rarely scatter from the surface. To consider surface scattering together with bulk scattering, we define

$$\rho_s^{\text{eff}} \equiv \rho - \rho_b, \tag{4.8}$$

the *effective* surface roughness contribution to resistivity, which is independent of ρ_b to first order (see Sec. 4.4).

To study the effect of individual spatial frequencies of roughness on resistivity, we perform a first order functional expansion on ρ_s^{eff}. We define the first variation in ρ_s^{eff} with respect to the PSD component at wavevector with magnitude k_0 as the response to a special PSD:

$$\rho_{(\zeta_{k_0})}^{\text{eff}} = \frac{l^2}{k_0}\frac{\delta\rho_s^{\text{eff}}}{\delta\zeta(k_0)}. \tag{4.9}$$

Here $\rho_{(\zeta_{k_0})}^{\text{eff}}$ is the response to a 2D PSD of the form

$$\zeta_{k_0}(\mathbf{k}) \equiv \frac{l^2\delta(|\mathbf{k}| - k_0)}{k_0}, \tag{4.10}$$

with $2\pi l^2$ the mean squared roughness of this PSD. The factor (l^2/k_0) in (4.9) is necessary for consistent units.

Consistent with the validity of (4.4) – (4.7) to first order in roughness, we perform a first order functional expansion of ρ_s^{eff} in ζ:

$$\rho_{(\zeta)}^{\text{eff}} = \int_0^\infty k_0 \, \frac{\rho_{(\zeta_{k_0})}^{\text{eff}}}{l^2} \, \zeta(k_0) \, dk_0 \; + \; O\left(\zeta^2\right) \tag{4.11}$$

Here the LHS is the resistivity from an arbitrary 2D isotropic PSD ζ, and $\rho_{(\zeta_{k_0})}^{\text{eff}}$ in the RHS is given by Eq. (4.9).

The angular harmonics for (4.10) are given by

$$\zeta_{k_0}^{(0)}(q, q') = \frac{2l^2}{\pi q q' \, |\sin \chi|} \, \theta\left(k_0 - |q - q'|\right) \, \theta(q + q' - k_0),$$

$$\zeta_{k_0}^{(1)}(q, q') = \zeta_{k_0}^{(0)}(q, q') \, \cos \chi,$$

where θ is the Heaviside step function, and the delta function sets the angle χ between the initial and final wavevectors

$$\cos \chi = \frac{q^2 + q'^2 - k_0^2}{2q q'}. \tag{4.12}$$

Our results for the functional derivative (4.9) for surface-only scattering $1/\tau_s \propto \rho_s$ and effective rate with bulk scattering $1/\tau_s^{\text{eff}} \propto \rho_s^{\text{eff}}$ are plotted in Figure 4.2.

We tested the relation (4.11) for several PSDs, including our fit to experimental surface roughness data (see below). For the experimental fit, we find (4.11) holds to 2% for a 25 nm film and 1% for 100 nm. We conclude that, for films thick enough that $\rho_s^{\text{eff}} \ll \rho$, Eq. (4.11) provides an effective calculation of resistivities.

We find that most of the range of k_0 fits

$$\frac{1}{\tau_{Fit}^{eff}} = \left(\frac{1.2 \cdot 10^{14}}{L} \text{nm/s}\right) \left(\frac{k}{k_F}\right)^{2.27} \left(2 - \frac{k}{k_F}\right)^{2.31}. \tag{4.13}$$

Although this fit fails for the very low-wavenumber tail of our results, this k_0 regime represents a very small part of the total k_0 range and also has the least impact on resistivity. So a good approximation for resistivity from arbitrary PSD ζ comes from substituting Eq. (4.13) in Eq. (4.11).
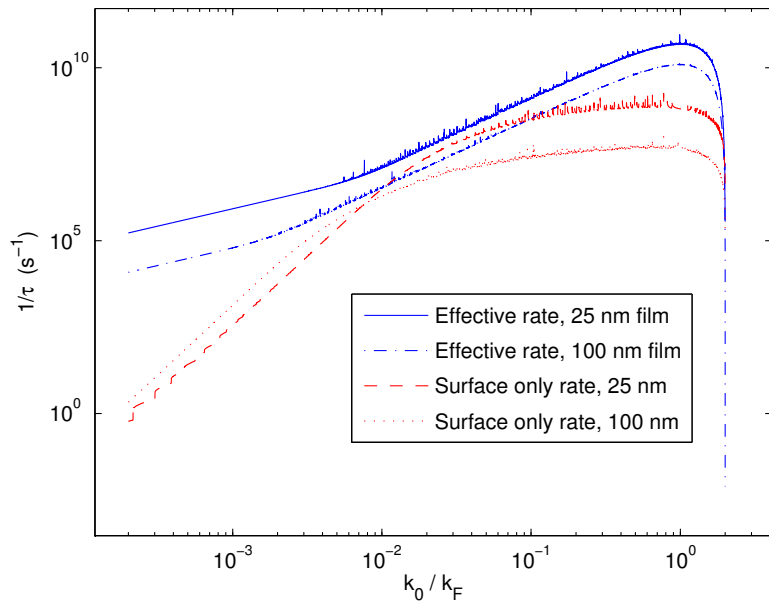
Figure 4.2: The momentum loss rate $1/\tau_s \propto \rho_s$ and $1/\tau_s^{\mathrm{eff}} \propto \rho_s^{\mathrm{eff}}$ in response to a single-frequency PSD (4.9), (4.10) in copper with $l = 10$ pm as a function of k_0. Note drastic breakdown of Matthiessen's rule, with $1/\tau_s^{\mathrm{eff}} \gg 1/\tau_s$.

4.3   Discussion

4.3.1   Quantization

For larger k_0 values, which dominate surface scattering, the thickness dependence of the *surface only* resistivity is $\rho_s \propto L^{-2}$, as in [51, 80]. But for large L, we expect ρ to approach the semiclassical result of Fuchs [24] and Sondheimer [73]:

$$\frac{\rho}{\rho_b} = \frac{\rho_b + \rho_s^{\text{eff}}}{\rho_b} = 1 + \frac{3}{8} \frac{\lambda_b}{L} (1 - p). \qquad (4.14)$$

Fig. 4.2 indeed shows $\rho_s^{\text{eff}} \propto k_0^2/L$ for most of the k_0 range.

For very small k_0 values, $\rho_s^{\text{eff}} \propto k_0/L^2$, while the surface-only rate actually increases with L, $\rho_s \propto L$. This can be explained by quantization. The subbands are spaced closest together for lowest j (see Figure 4.1). So for $k_0 < \sqrt{3}\pi/(k_F L)$, there is no scattering between higher order subbands. As k_0 becomes smaller, the cutoff subband below which interband transitions due to surface roughness is forbidden gets lower and lower. For extremely small k_0 ($k_0 < 10^{-5} k_F$ for this plot), only intraband scattering at angles $\sim k_0/k_F$ is allowed, and Eq. (4.10) behaves much like a smooth surface. This limit can be derived analytically (see Section 4.4). The left side of Fig. 4.2 is the regime where interband transitions are being introduced.

For ρ_s, an increase in L *decreases* the spacing between k_j values, introducing interband transitions between low j states where the spacing is smallest. Physically, this couples states traveling nearly parallel to the film surface with other states that interact much more strongly with the surface, providing a mechanism to increase ρ_s with L.

For ρ_s^{eff}, in contrast, electrons in low j states are already frequently scattered by bulk scattering. For small k_0, only intraband scattering is possible, so there are always two final states and $\rho_s^{\text{eff}} \propto k_0/L^2$. At higher k_0, the number of available final subbands becomes proportional to L, so $\rho_s^{\text{eff}} \propto k_0^2/L$.

4.3.2 Surface Scattering for PSDs Measured in Real Films

As can be seen from Fig. 4.2, spatial frequencies near k_F (shortest wavelengths) have the strongest momentum loss, but the impact on conductivity depends on the actual roughness PSD of metal films and wires. Any attempts to improve conductivity will benefit from a knowledge of which components of surface roughness give the most improvement for the resources spent. Theoretical calculations often assume a Gaussian roughness spectrum, but experiments show that many PSD forms are present depending on the wire deposition conditions [51], and that real PSDs can fall of more slowly than Gaussian [22]. Unfortunately, the experimental literature on surface roughness spectra for metals is limited and focuses on relatively large length scales. Thus, we look to other materials. Feenstra *et al.* [22] observed that 1D STM scans of InAs/GaSb superlattice interfaces showed Lorentzian distributions,

$$\zeta(k) = \frac{2\Lambda\Delta^2}{(1 + k^2\Lambda^2)}.$$

For isotropic roughness, this corresponds to a 2D PSD of the form

$$\zeta(k) = \frac{2\pi\Lambda^2\Delta^2}{(1 + k^2\Lambda^2)^{3/2}}, \tag{4.15}$$

where Λ is the correlation length of surface roughness and $2\pi\Delta^2$ is the mean squared roughness (statistical variance in surface height). Eq. (4.15) also fits the AFM results of Moseler *et al.* [55] for Cu films with $\Lambda = 18$ nm, $\Delta = 1.8$ Å, as shown in Fig. 4.3. Other experiments on copper films confirm a correlation length of $\sim$20 nm [35]. We also fit [55]'s data to a Gaussian PSD, as shown in the figure. Because measurements at high spatial frequencies (which have a particularly strong effect on scattering) are lacking, our goal is to extrapolate from these fits[1].

We can use extrapolations from the Moseler data to calculate the resistivity, or

---

[1]Ref. [22]'s STM of InAs/GaSb, which extends to wavevectors of 10 nm^{-1} compared to [55]'s AFM up to 0.1 nm^{-1}, supports the fit in Eq. (4.15). Note that the flattening near the highest frequency is due to the finite sampling interval used in [55].
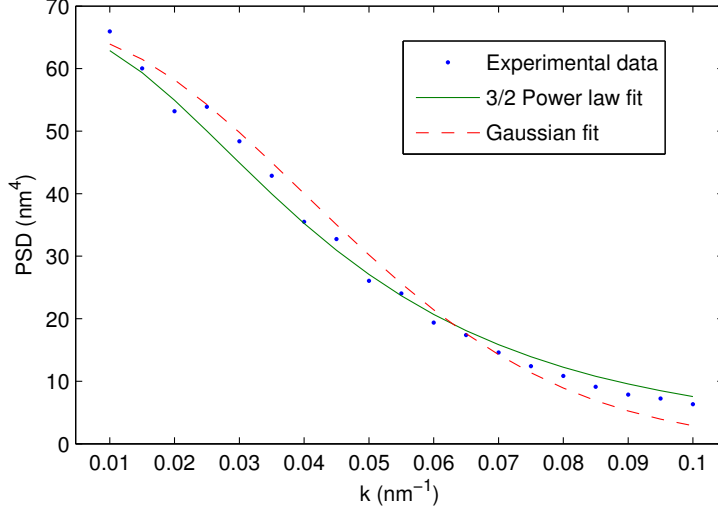
Figure 4.3: Normalized roughness spectra for Cu films [55] compared to fits to Eq. (4.15) with correlation length $\Lambda = 18$ nm and Gaussian with $\Lambda = 1/\sigma = 25$ nm. Both forms fit the available data, but give very different predictions of fall-off in roughness at higher spatial frequencies.

equivalently the specular fraction p. Substituting (4.11) in (6.1):

$$p = 1 - \frac{8}{3}\frac{L}{\lambda_b}\int_0^{2k_F} k_0\,\zeta\left(k_0\right)\,\frac{\tau_b}{l^2\,\tau_s^{\text{eff}}\left(k_0\right)}\,dk_0, \tag{4.16}$$

which (for $L >$100 nm) is independent of L. We find p values of essentially 1 for the Gaussian PSD and $p = 0.96$ $(1 - p = 0.04)$ for Eq. (4.15). We get the same results when we use the full PSDs directly as in Eqs. (4.4) – (4.7)

The fact that our analysis predicts highly specular $(p \sim 1)$ surface scattering for technologically-achievable surface roughness suggests that surface roughness scattering is a surmountable barrier to high conductivity. We can extract the most important components of roughness, taking into account both the relative strength of scattering and the observed roughness spectra. The effective diffuse scattering rate as a function of spatial frequency is shown in Fig. 4.4. More accurate measurements of the high frequency portion of the PSD are clearly needed, as the frequencies above 0.1 nm^{-1} are most critical to conductivity degradation.
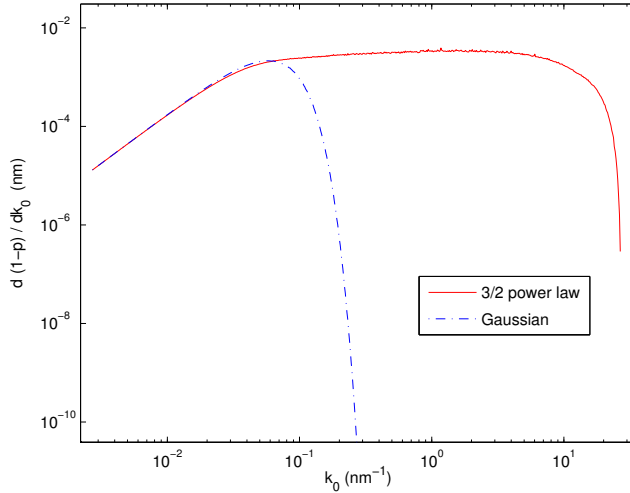
Figure 4.4: Integrand of Eq. (4.16) with PSDs from Fig. 4.3. Diffuse fraction $(1-p) \propto \rho_s^{\text{eff}}$ is the area under the (1D) curve as shown. The tail of the PSD is seen to have a major effect. The most important roughness components are $0.1 \, \text{nm}^{-1} < k_0 < k_F = 13.6 \, \text{nm}^{-1}$ for Eq. (4.15) and $k_0 \approx 0.05 \, \text{nm}^{-1}$ for Gaussian.

Another way to understand these results is to note that for (4.15) with $\Lambda = 18$ nm, $p = 90\%$ corresponds to an RMS roughness of 7 Å, compared to experimental measurements in the range $2 - 11$ Å; see [14, 61, 84] and refs. therein.

4.3.3 Technological Impact

The experimental literature is somewhat mixed on the relative importance of surface scattering. Many results suggest that the observed resistivity increase is dominated by grain boundary rather than surface scattering [20, 74, 49, 46, 47, 83, 29], while some extract values of p near 0 (diffuse rather than specular scattering) [61, 84]. As we have seen, p depends strongly $(O(l^2))$ on RMS roughness, which in turn depends on anneal times, deposition conditions, and other process variables. Another interesting explanation for this discrepancy may come from the experiment of Rossnagel et al. [65], which we will discuss further in Chapter 6. They found that conductivity

decreased strongly upon the deposition of an ultrathin Ta layer on top of a Cu film, but that the conductivity recovered when the Ta film was exposed to air, thereby oxidizing to become insulating. These observations suggest that thin barrier/adhesion layers rather than surface/interface roughness may be causing the apparent diffuse surface scattering.

To summarize, we have found that bulk scattering can be included in quantum models of surface scattering by adding τ^{-1} matrices. This leads to violation of Mathiessen's rule, but an effective surface resistivity ρ_s^{eff} independent of bulk scattering can be extracted. The resistivity from individual wavelengths of roughness can be convolved with roughness PSD to get ρ_s^{eff} for arbitrary surface. Our analysis suggests that roughness with wavelength within 1-2 orders of magnitude of the Fermi wavelength is the most critical for conductivity degradation.

The remainder of this chapter presents analytical approximations useful for understanding our results and performing simplified calculations.

4.4 Analytical Approximations

4.4.1 Expansion for $\rho_s \ll \rho_b$

We show by expanding in

$$\tau_b \tau_s^{-1} = \frac{v_F}{\lambda_b} \, \tau_s^{-1}$$

that

$$\frac{1}{\tau_s^{\text{eff}}} = \frac{\langle k, \tau_s^{-1} k \rangle}{k^2} + O\left(\frac{v_F \tau_s^{-1}}{\lambda_b}\right)^2. \tag{4.17}$$

Here we borrow the notation of inner product,

$$\langle k, \tau_s^{-1} k \rangle \equiv \sum_{ij} k_i \, (\tau_s)_{ij}^{-1} \, k_j,$$

and $k^2 \equiv \sum_i k_i^2$. Note that Eq. (4.17) is *independent of bulk scattering* to first order. Moreover, it makes it unnecessary to invert $\tau^{-1} = \tau_b^{-1} + \tau_s^{-1}$ to find conductivity by

Eq. (4.7) and then take the reciprocal to find resistivity. It also provides additional justification for Eq. (4.11).

First we do the matrix inversion to first order. One can verify by substitution that

$$\tau = \left(\tau^{-1}\right)^{-1} = \tau_b \left[1 + \tau_b \tau_s^{-1}\right]^{-1} = \tau_b \left[1 - \tau_b \tau_s^{-1} + O\left(\tau_b \tau_s^{-1}\right)^2\right].$$

Then, from Eq. (4.7),

$$\tau = \frac{1}{2\pi n L} \langle k, \ \tau \ k \rangle,$$

and

$$1/\tau_s^{\mathrm{eff}} = \frac{1}{\tau} - \frac{1}{\tau_b} \sim \frac{1}{\tau_b} \left\{ \frac{2\pi n L}{\langle k, \ [1 - \tau_b \tau_s^{-1}] \ k \rangle} - 1 \right\} \sim \frac{1}{\tau_b} \left\{ \frac{2\pi n L}{k^2} (1 + \frac{\langle k, \ \tau_b \tau_s^{-1} \ k \rangle}{k^2}) - 1 \right\}.$$

The derivation is completed by noting from Eq. (4.1) that

$$k_j = k_F \sqrt{1 - j^2/\kappa^2},$$

where $\kappa \equiv k_F L/\pi$, so

$$k^2 = k_F^2 \, n_c \left(1 - \frac{(n_c + 1)(2n_c + 1)}{6\kappa^2}\right) \overset{k_F L \gg 1}{\longrightarrow} \frac{2 \, k_F^3 L}{3\pi}$$

where $n_c = \mathrm{Int}\{\kappa\}$ is the total number of subbands, and in the free-electron model, $n = k_F^3/3\pi^2$.

Eq. (4.17) holds very well for our 25 nm calculation, for which $n_c \sim 100$. Note that Eq. (4.17) is by no means the same as the *surface-only* momentum loss rate, $1/\tau_s \propto k^2/\langle k, \tau_s k \rangle$, which would be the surface scattering rate in the *absence* of bulk scattering. Eq. (4.17) is a first-order expansion in the presence of very large bulk scattering.

4.4.2   *Analytical Derivation of Low-k_0 Limit of ρ_s^{eff}*

Here we derive the ρ_s^{eff} behavior when k_0 is small enough that τ_s^{-1} is completely diagonal or increasing L introduces interband transitions. When the wavelength of

surface roughness is long enough that τ_s^{-1} is completely diagonal, the surface is too smooth to allow interband transitions. This happens for

$$k_0 < k_1 - k_2 = k_F \left(\sqrt{1 - 1/\kappa^2} - \sqrt{1 - 4/\kappa^2} \right) \approx \frac{3k_F}{2\kappa^2} \sim 10^{-5} \, k_F.$$

In this regime, only small-angle scattering within the subband is allowed. From Eq. (4.12), we find

$$\cos \chi_{jj} = 1 - \frac{k_0^2}{2 \, k_j^2},$$

giving

$$\chi_{jj} = k_0/k_j \sim 10^{-5}. \tag{4.18}$$

Then we can derive

$$W_{ij} = \frac{1}{mL^2} \left(\frac{i\pi}{L} \right)^2 \left(\frac{j\pi}{L} \right)^2 \zeta(k_i, k_j),$$

and

$$\zeta \sim \frac{2l^2}{k_i \, k_j \sin \chi_{ij}}.$$

Even when a few off-diagonal elements are present, these will still be dominated by the diagonal ones because of the small χ.

According to Eq. (4.5), τ_s^{-1} is a difference of harmonics of W, so

$$1/\tau_{ii}^s \sim \frac{\chi^2}{2} \frac{\hbar}{m} W_{ii}^0, \tag{4.19}$$

since $1 - \cos \chi \approx \chi^2/2$. Substituting in our expressions for W, ζ, and χ, we find

$$1/\tau_{ii}^s \sim \frac{\hbar}{m} \chi \, k_F^4 \left(\frac{i}{\kappa} \right)^4 \frac{l^2}{k_i^2 \, L^2} \sim .$$

Then

$$\langle k, \, 1/\tau^s \, k \rangle \sim \sum_i k_i^2 1/\tau_{ii} \sim \frac{\hbar}{m} \frac{k_F^3 l^2 \, k_0}{L^2} \kappa \int \frac{x^4 dx}{\sqrt{1 - x^2}},$$

where in the last step we approximate summation with integration over $x \equiv i/\kappa$.

Using Eq. (4.17), we find

$$1/\tau_s^{\text{eff}} \sim \frac{9\pi \, \hbar}{32 \, m} \frac{l^2 k_F \, k_0}{L^2} \propto \frac{k_0}{L^2}. \tag{4.20}$$

Chapter 5

GRAIN BOUNDARY SCATTERING

This chapter presents simulation work on grain boundary scattering that I did at Intel Corporation in collaboration with Seongjun Park, Michael Haverty, and Sadasivan Shankar.

The goal of this chapter is to present the first microscopic predictions of grain boundary reflectivity in metals and to compare these results with experimental data. We also analyze the structure of grain boundaries and determine what aspect of their structure has the greatest effect on scattering. Specifically, we investigate the relative importance of atomic displacements at the boundary and the change in orientation from one grain to the other.

5.1 Method

We use the Non-Equilibrium Green's Function (NEGF) method with the Landauer formalism in this work [16] (see Chapter 3). As described in Section 3.3.6, we use the commercial code Atomistix to perform our transmission simulations.

In this chapter, we investigate reflection probability R for various structures. In our notation, the transmission $\bar{T} = Gh/2e^2 = (1-R)M(E_F)$, where G is conductance and $M(E_F)$ is the number of forward-moving modes with $E = E_F$ (see Section 3.2). We present computer simulations using Density Functional Theory [38, 37] (Section 3.4) to compute in NEGF (Section 3.3) the transmission $\bar{T}$ in various grain boundary systems at 0 K in both Cu and Ag.

We perform the relaxation with the Vienna Ab-Initio Simulation Package [39] within LDA, using augmented wave pseudopotentials [40] and periodic boundary con-
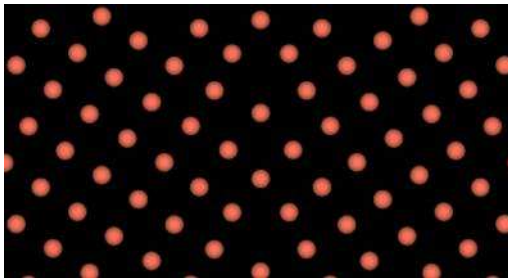
Figure 5.1: Structure used for transmission simulation of twin (210)/(120) boundary in Cu (relaxed). In all figures, transmission is rightward as shown.
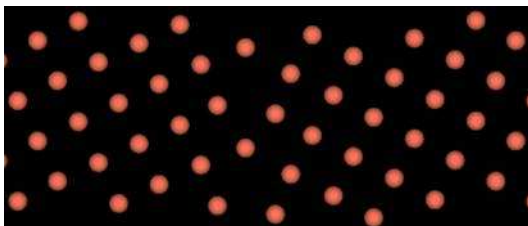
Figure 5.2: Twin (320)/(230) boundary in Cu (relaxed).

ditions. Due to the periodic boundary condition, we use at least 10 atomic layers for both sides of grain to avoid the effect of repeating images on the configurations of grain boundaries. We do not relax the structures for simulations intended to study controlled atomic defects, such as vacancies and disorder as described below.

We simulate twin (Coincidence Site Lattice, or CSL) and non-twin grain boundaries in two FCC (Face Centered Cubic) crystal structure metals, Cu and Ag. We prepare twin boundaries for the two angles with smallest supercells, corresponding to (210)/(120) and (320)/(230), as shown in figures 5.1 and 5.2. We also prepare non-twin boundaries for (111)/(110), (110)/(100), and (111)/(100) as demonstrated in Figure 5.3.

5.2 Results

The reflectivity simulation results are summarized in Table 5.1.

Table 5.1: Summary of simulation results. All systems are periodic in plane normal to transmission direction.

System	Relaxed?	R_{Cu} (%)	R_{Ag} (%)
Twin (210)/(120)	Y	17	12
Twin (320)/(230)	Y	13	14
Non-Twin (111)/(110)	Y	-	36
Non-Twin (110)/(100)	Y	-	46
Non-Twin (111)/(100)	Y	19	16
Vacancy $(39.2 \text{ Å}^2)^{-1}$	N	8.3	-
Vacancy $(19.6 \text{ Å}^2)^{-1}$	N	11	-
Disorder 2 layers	N	6.9	-
Disorder 4 layers	N	22	-
Disorder 6 layers	N	24	-
Disorder 8 layers	N	27	-

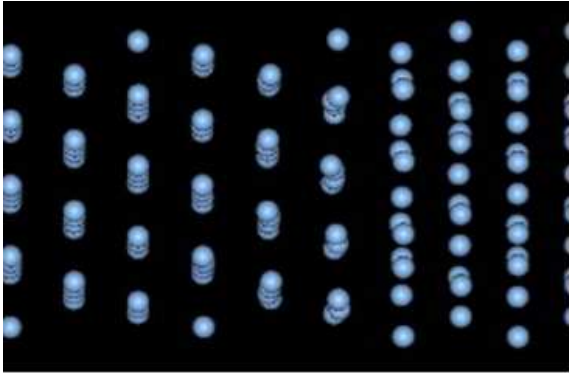Figure 5.3: Non-twin (100)/(110) boundary in Ag (relaxed).

5.3 Comparison to experiment

In the literature, the Mayadas-Shatzkes model (Chapter 2) is the most widely used analytical model to extract grain boundary reflectivity from experimental data. The MS model describes metal conductivity as a function of boundary reflectivity R and grain size D. The MS model agrees with an even simpler model we constructed based on the Landauer formula [16] (section 3.2) and the assumption of an average grain boundary reflection probability R. For resistivity of a conductor with bulk scattering of mean free path λ_b and grain boundary scattering, both theories give

$$\frac{\rho}{\rho_b} \approx 1 + \kappa \, \frac{\lambda_b}{D} \, \frac{R}{1-R} \tag{5.1}$$

to lowest order in $R/(1-R)$. Here $\kappa = hA/(2M(E_F)\lambda_b \, \rho_b \, e^2) \approx 4/3$ in our theory and 1.39 in MS [20]. Thus, at room temperature and D = 45 nm, a grain boundary reflectivity of 20% increases resistivity by $\sim$31% over the bulk value. Our results from a direct simulation of multiple grain boundaries call into question the MS model assumption of a single parameter R averaged over all types of boundaries in the sample, as we will describe later. However, we compare our results to experimental R values extracted using MS, as it is currently the standard model of ρ as a function of microscopic properties. We compare to experimental results at 5 K where the effect of bulk scattering is minimal and to compare more directly to our 0 K results.

Although Cu is more important for integrated circuits, better experimental data is available on Ag. The low temperature experiments indicated $R \approx 25\%$ for Ag [20] in comparison to our values $R \approx 12\%$ for twin boundaries and R from 16% to 46% for non-twin boundaries (Table 5.1). A survey of experimental results indicates R for Cu and Ag in the range from 24% to 46% [6, 9, 18, 19, 28, 21, 44, 27, 48, 67, 68, 69, 81, 85].

A review of the literature identified two experimental references that measured grain boundary resistance directly in a metal. Schneider *et al* [68, 69] measured reflectivity for single grain boundaries in Au (a material similar to Cu and Ag), and found reflectivity in the range 0.7 to 0.9, depending on orientation. Nakamichi [57]

54

measured specific interface resistivity $\rho_{gb} = R_{gb}A$ (where R_{gb} is resistance) in Al for various types of grain boundaries. To compute reflectivity, we estimate the ballistic conductance per unit area G/A for Al by Eq. (5.3) below assuming a spherical Fermi surface. We then compute reflectivity for Nakamichi's results with

$$R = 1 - \frac{A/G}{(\rho_{gb} + A/G)}. \tag{5.2}$$

Aggregating Nakamichi's results and analyzing according to this expression, we find most of the measured twin boundary results in the range $R = 0\%$ to 27% and non-twin results in the range $R = 36\%$ to 51%. The range of reflectivity variations agrees with our findings, although it is unclear how well one should expect R to agree across metals.

5.4   Determinants of reflectivity

Real grain boundaries in metals are not necessarily 2-dimensional plane defects as in our constructed twin and non-twin models. Their structure will likely be three-dimensional in nature due to pile-up of dislocations, vacancies, and/or impurities at the boundary. Also the boundaries often will not be orthogonal to the transmission direction. To understand better the causes of reflectivity and the impact of boundaries' three-dimensional structure, we present simulations isolating particular features of grain boundaries. Since a grain boundary is the interface between two crystallites, there are two broad categories of scattering that could occur: 1) scattering caused by the misaligned crystal orientation of the two grains, a category we refer to as *orientation effects*; and 2) the atomic structure in the interface itself, which we call *atomic position effects*. We present simulations and analytical arguments to quantify the relative contribution of these two effects.

5.4.1 Orientation effects

We wish to understand the contribution to scattering from the change in orientation across grains, R_s. A perfect (unrelaxed) twin boundary has mirror symmetry across the boundary plane, and therefore identical bases of Bloch states on either side. Moreover, an ideal CSL has a boundary of zero thickness, so the only possible cause of scattering is the sudden change in orientation. We therefore estimate the orientation effect by the results of our transmission simulations for unrelaxed CSLs (not presented above), $R \sim 15\%$.

In a non-twin boundary, the interface is not as sharp and the forward moving states in the two grains should be different. One might expect increased reflection due to the difference in transmission across the two grains. We therefore simulate transmission in several different grain orientations, with results presented in Table 5.2. We estimate the orientation effect by the relative difference $|\Delta T|/T$ in transmission across the boundary. (This is by analogy to a simple 1D quantum potential step, $R = (\Delta k/(k + k')^2)$, where k and k' are the momenta on either side of the step.) We find that transmission in the (100) and (111) direction is similar, while transmission in the (110) direction is 22% higher. We find an intermediate value of transmission for two intermediate orientations (210) and (320) between (100) and (110). This shows a large dependence of T on orientation for a perfect crystal, although we expect that bulk scattering would diminish the orientation effect.

To confirm this large dependence of T on orientation we compare the simulation results with an analytical estimate of T as a function of orientation in Cu. In the Landauer formulation [16], the resistivity in perfect metal crystals at absolute zero (ballistic conductors) is contact resistance. This is caused by the finite number of transverse modes per unit area with cutoff less than the Fermi energy (see Section 3.2). The number of modes is equivalent to the cross sectional area of the Fermi

Table 5.2: Cu ballistic transmission *vs.* orientation. T/A values for Ag are generally scaled down from the ones presented in this talbe by $(a_{\text{Ag}}/a_{\text{Cu}})^2 = 1.28$.

Orientation	T/A (Å^{-2})	Normalized to $T(100)/A$ (%)
(100)	0.1388	100
(111)	0.1362	98
(110)	0.1701	122
(210)	0.1462	105
(320)	0.1470	106

surface in a plane normal to the transmission direction:

$$\frac{T_c}{A} = \frac{M(E_F)}{A} = \frac{1}{(2\pi)^2} \int \hat{n_\perp} \cdot \hat{z} \; \mathbf{d}^2 k_{||} \tag{5.3}$$

where T_c is contact transmission, $\hat{n_\perp}$ is a unit vector normal to the Fermi surface, $\hat{z}$ is the transmission direction, and the domain is the set of points on the Fermi surface with $\hat{n_\perp} \cdot \hat{z} \geq 0$. Evaluating this expression with a spherical Fermi surface gives $M(E_F)/A = 0.1472$ Å^{-2} for copper, which is within the range of simulated values in Table 5.2.

This integral may be evaluated numerically for different directions z. The deviations from a spherical Fermi surface then give the effect of grain orientation on ballistic transmission. For a non-ballistic conductor, the orientation effect would be muted. This calculation has been carried out in [82], giving $T(110)/T(100) = 1.07$ and $T(111) \approx T(100)$. This is in qualitative agreement but in poor quantitative agreement with our results, which show a much stronger orientation dependence.

5.4.2   Atomic position effects

We isolate the atomic position in the interface by simulating various idealized models to get an idea of the magnitude of the effect, R_a. Our underlying assumption is that
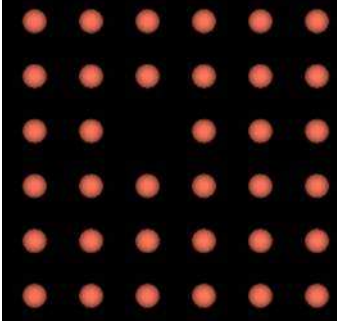
Figure 5.4: System with plane of vacancies at density $(39\ \text{Å}^2)^{-1}$.

total reflectivity from atomic position in the boundary can be decomposed as a sum of individual defect reflectivities:

$$R_a = \sum_i R_{a,i}. \tag{5.4}$$

We model vacancies in grain boundaries by simulating structures with a single interface containing vacancies (see Fig. 5.4). We examine two different vacancy densities, one or two vacancies per 39 Å^2. Results are 8% and 16%, scaling linearly for the densities of $1/(39\text{Å}^2)$ and $2/(39\text{Å}^2)$. Analytically, one expects scattering cross section of the order of magnitude of the area of the missing atoms. The result with one missing atom per 39 Å^2 gives an analytical estimate R = 1/12 = 8.3%. This is good agreement for an order of magnitude estimate. It also supports our assumption that the total reflectivity is the sum of individual defect reflectivities.

To investigate the effect of atomic position on reflectivity, we simulate layers of disordered Cu atoms as shown in Fig. 5.5 to isolate the effect of crystalline order on conduction. The disordered atoms are displaced by normally distributed random vectors with RMS magnitude 0.24 Å or 0.70 Å. We change the number n of such layers and expect from theory that $R \approx n/(n + n_0)$ with a constant n_0, since in a metal, localization length is long compared to phase coherence length (and our system size) [16]. We summarize the results in Figure 5.6. This plot has roughly the
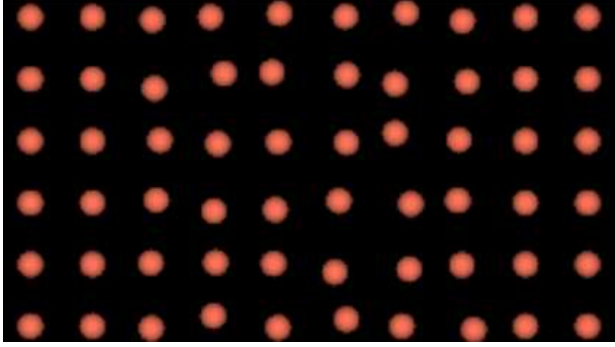
58

Figure 5.5: System with 6 disordered layers (layers 3–8 of those shown). Alternate atoms are in inequivalent planes.

expected behavior with $n_0 \approx 50$ for the 0.24 Å roughness and $n_0 \approx 8.8$ for the 0.7 Å roughness. These disordered region simulations give insight into the effect of non-linear boundaries on reflectivity, and show that the impact of non-lattice site atomic positions is significant.

These structures are not the only possible departures from crystalline order, but provide an estimate of the magnitude of the atomic position effect:

$$R_a \sim (8\%) \, d_d \, (39 \, \text{Å}^2),$$

with d_d the defect area density in the boundary, and $5\% < R_a < 30\%$, depending on the magnitude of disorder in the boundary. The objective of these estimates is to approximately predict R_a, rather than to provide a complete theory. Both estimates reflect a strong dependence of grain boundary reflectivity on atomic position (e.g. gaps, relaxation).

5.5 *Validity of Mayadas-Shatzkes model*

We also attempted to check the validity of the Mayadas-Shatzkes model assumptions using atomic model systems of multiple grain boundaries. Our simulations include two (210)/(120) twin boundaries separated by from 2.7 nm to 4.6 nm. We verified
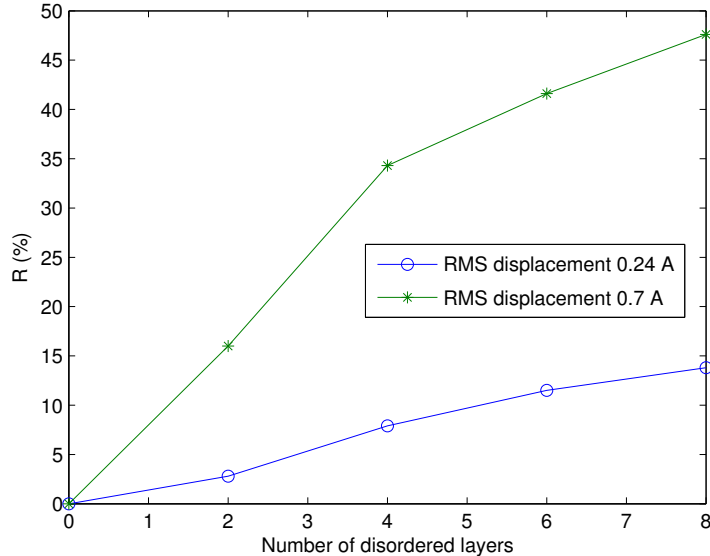
Figure 5.6: Total reflection probability R *vs.* number n of disordered layers. Systems with smaller n have a subset of the disordered region present in systems with larger n. There is significant variability evident due to magnitude of displacement.

that the results change little for increasing boundary separation (grain size) in order to ensure that the boundaries do not interact.

Although this differs markedly from the infinite system with grain sizes $\sim$45 nm assumed above, we can compare the results to the Landauer transport model for just two boundaries. This theory gives the total reflectivity as $R_T = 2R/(1 + R)$, where R is the reflectivity of a single boundary [16]. Using the results from Table 5.1, we anticipate $R_T = 29\%$ for Cu and $R_T = 21\%$ for Ag. We find our results differ from the smallest to largest grain size as shown in Table 5.3. We attribute this change in reflectivity to interactions between boundaries. We further find that the simulation-predicted R is lower than that predicted by the Landauer theory for two boundaries. This may be explained by the fact that reflectivity depends strongly on initial momentum. The first boundary may act as a filter that lets only those states with highest transmission through to the second boundary. However, this needs

Table 5.3: Total grain reflectivity of two twin grain boundaries with various grain sizes (in units of lattice constant a) for Cu and Ag. The Landauer prediction would be $R_T = 29\%$ for Cu and $R_T = 21\%$ for Ag for all grain sizes large enough to avoid interaction between boundaries.

Grain size / a	R_T for Cu (%)	R_T for Ag (%)
6.71	23.6	19.3
8.94	25.8	14.7
11.16	24.5	17.4

further studies for a better understanding. Also, it is unclear how bulk scattering and boundary type variety would affect this explanation. The MS model also fails to consider scattering of electrons upon reflection or transmission.

5.6 Effect on Resistivity

The damascene process is capable of depositing Cu interconnects with grain size larger than the line thickness. For example, Geiss and Read [25] report an average grain diameter of 315 nm for 100 nm damascene Cu lines. Similarly, Paik *et al.* [58] measured grain sizes in the range 125 – 275 nm for ∼170 nm line thickness. Both Carreau *et al.* [4] and Steinhögl *et al.* [75] measured somewhat smaller grains for thinner damascene-deposited interconnects (see Figure 5.7), and observed that grain size does indeed scale with thickness for the thinnest wires.

Using Eq. (5.1), the results of Geiss and Read give a resistivity augmentation of 17% for average $R = 50\%$, and 4% if the average of R is only 20%. On the other hand, for a grain size of ∼40 nm as observed by [4] for line widths of ∼70 nm, Eq. (5.1) gives an augmentation 8 times as high, or 35% for $R = 20\%$. Clearly, the importance of grain boundary scattering depends strongly on grain size. Global interconnects, which are most important in RC delay times (see Chapter 1), can be significantly thicker than local ones, and therefore may have larger average grain sizes. On the

other hand, local interconnects have a total length that scales more strongly with the number of transistors, and therefore have an important effect on power loss. Since local interconnects must scale in thickness with minimum feature size, the smaller grain sizes for very thin wires observed by Carreau *et al.* may be more relevant for power loss.

5.7 Summary

We have presented the first simulations of reflectivity for relaxed twin and non-twin grain boundaries in Cu and Ag. Our results agree with the experimental reported range of reflectivity [6, 9, 18, 19, 28, 21, 44, 27, 48, 67, 68, 69, 81, 85] and with the individual boundary measurements of Nakamichi [57]. To gain insight into the mechanisms of grain boundary reflectivity and the impact of the non-planarity of real grain boundaries, we also investigated the effect of vacancies, orientation, and disorder. We find that all three contribute significantly to reflectivity. Our predicted dependence of reflectivity on grain boundary type and isolated vacancy, orientation, and disorder effects explains why the experimentally reported range of reflectivity varies widely. In probing the utility and extendibility of the Mayadas-Shatkes model we find that the assumption of a one-parameter reflectivity averaged over all grain boundaries and initial states fails to accurately estimate reflectivity from multiple grain boundaries that are closely spaced, but may be reasonable for grain boundaries with spacing greater than the mean free path. Improvements in the analytical models to account for the discrepancy in additivity of the reflectivity of grain boundaries and the impact of grain boundary type and non-planarity are needed.
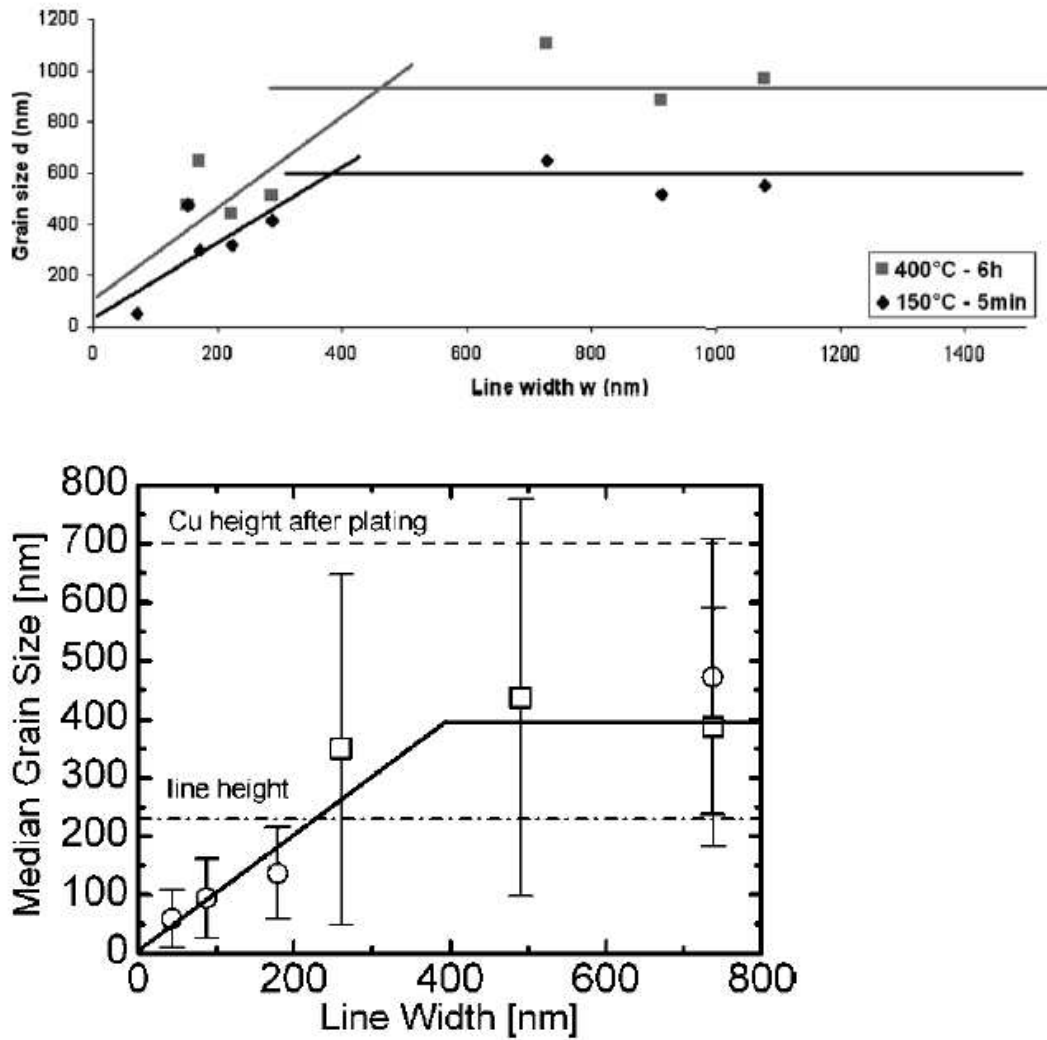
Figure 5.7: Grain sizes in damascene-deposited Cu measured by Carreau *et al.* [4] for two different annealing conditions (first figure) and by Steinhögl *et al.* [75] for 230 nm line height (second figure). Both figures show a linear relationship at the smallest line widths.

Chapter 6

INTERFACE SCATTERING

In this chapter, we present some of the first calculations of scattering and transmission at the interface between Cu nanowires and their liner layers.

6.1 Method

We model the liner layer by the most common form of Ta deposited epitaxially on Cu, $\beta-$Ta [62, 41], which has a bulk resistivity of (200 ± 20) $\mu\Omega\cdot$ cm [62, 32] or even 250 $\mu\Omega\cdot$ cm [65], compared to 1.7 $\mu\Omega\cdot$ cm for Cu.

The structure of $\beta-$Ta [41] is a tetragonal lattice with constants $a = 10.2$ Å and $c = 5.3$ Å. In the $z-$direction (corresponding to the c lattice parameter), it contains four equally spaced layers alternating between four regularly spaced Ta atoms and 11 atoms arranged in a pseudo-hexagonal pattern (see Figure 6.1). The $\beta-$Ta unit cell contains a total of 30 atoms. The $\beta-$Ta can be grown epitaxially on Cu (111) surfaces with a relative strain in each a direction of approximately 7% [41, 36, 43], causing the pseudo-hexagons in Ta to match those in Cu.

We have set up such an epitaxial system for relaxation with the Vienna Ab-initio Simulation Package [39]. Our system contains a total of 56 Ta and 64 Cu atoms. The Ta terminates with an 11-atom Ta layer, interfacing with a partial Cu layer with 4 atoms, followed by full Cu (111) layers. We have fully relaxed this system keeping the bottom Ta layer fixed but leaving the top Cu layer free to adjust in the z dimension. This allowed the total interface size and $z-$spacing among layers to relax. The variation in $z-$position among Cu atoms within the topmost layer after relaxation was small compared to the layer spacing.
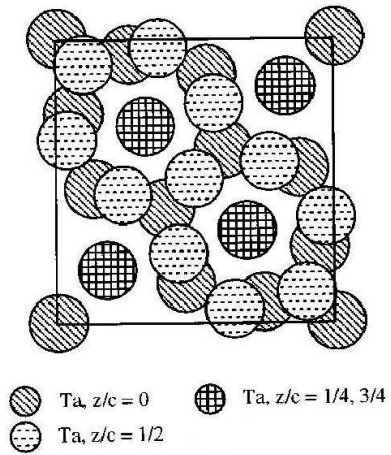
Figure 6.1: Structure of β-Ta. Figure taken from Ref. [41].
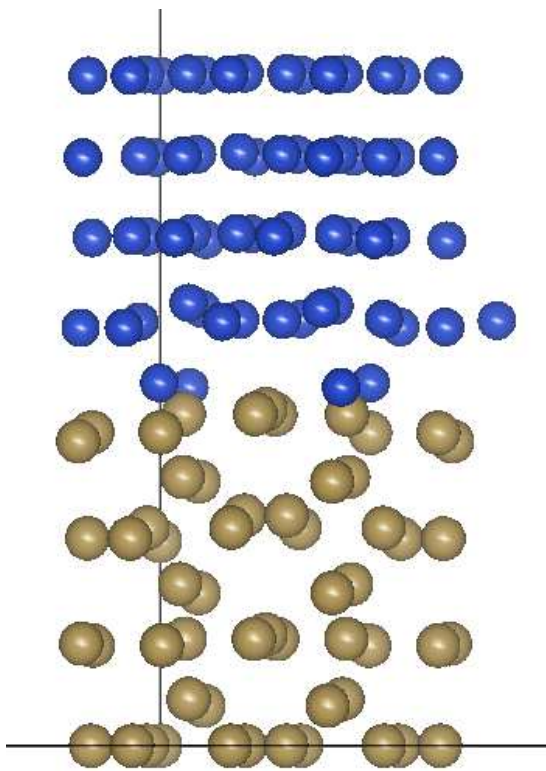

Figure 6.2: The relaxed interface. Top five layers are Cu, bottom (ring-like) layers are Ta.

To simulate transmission across a Cu/Ta interface, we replaced $z-$coordinates of the topmost Cu layer by their average, leaving ideal Cu and strained $\beta-$Ta layers at the two ends of the interface. The resulting system is shown in Figure 6.2. We then set up a transmission simulation using the relaxed interface as a scattering region and matching the perfect Cu and Ta layers to electrodes made of ideal lattices of the respective materials. We have used the Non-Equilibrium Green's Function Method (Section 3.3) to simulate dynamical transmission across interfaces with Atomistix (Sec. 3.3.6), as in our work on grain boundaries.

6.2 Results

The resulting simulation showed that overall transmission probability at the Fermi energy $T(E_F) = 0.22$ for electrons originating in Cu and 0.39 for those originating in Ta[1].

6.2.1 Effect on Conduction

We can estimate the effect on conduction in Cu using a simple model based on the surface scattering models of Fuchs [24] and Sondheimer [73]. Although the liner layer represents a parallel conductance to the Cu wire, the high resistivity of $\beta-$Ta makes this almost negligible [65]. Instead, we consider the effect of electrons entering Ta and rapidly losing their net momentum. When wire thickness t is not too much less than mean free path λ so that multiple scattering can be neglected, the proportion of carriers affected by interactions with the surface is

$$\frac{CP\lambda}{A},$$

---

[1]Here transmission probability is $T \equiv \bar{T}/M$. Note that conduction electron density, and therefore the number of modes M, is different in the two materials. As usual, $\bar{T}$ is reciprocal (Eq. (3.21)) and the *net* current is zero across the unbiased interface after the vacuum levels have adjusted to equilibrate the Fermi levels. A space charge region forms at the interface, analogous to that at a PN-junction, to bring about this equilibrium.

where C is a dimensionless constant, and P and A are the perimeter and area, respectively, of the wire cross-section [73]. Comparison with more detailed semi-classical calculations gives $C = 3/16$ [73]. Then the resistivity augmentation over bulk is given by

$$\frac{\rho}{\rho_b} = 1 + \frac{3\lambda P}{16A}(1 - p), \tag{6.1}$$

where $1 - p$ is the proportion of electrons that lose their momentum on interaction with the surface [73].

Although Fuchs and Sondheimer originally considered these models in the context of surface roughness, we generalize to a steady state where electrons diffuse into Ta, rapidly lose their net momentum, and diffuse back with zero drift in the conduction direction. This steady-state picture is valid when the Ta thickness is large compared with the bulk mean free path λ_{Ta} in β-Ta, which we estimate as follows. The product of Sharvin (ballistic) conductance and bulk resistivity gives a length scale of order the bulk mean free path [16], a relation that holds to within 40% for Cu[2]. For β-Ta, our simulations of transmission in perfect β-Ta crystals combined with bulk resistivity measurements suggest $\lambda_{\text{Ta}} \approx 5$ – 11 Å (compared to $\lambda = 39$ nm in Cu)[3]. In this picture, every electron that transmits into Ta is on average replaced with one from Ta with ~zero net conduction momentum, so it is identical to a diffuse scattering event. Then $(1-p)$ would be given approximately by the diffuse probability $1-p = 0.04$ we calculated for a rough Cu surface (Chapter 4) plus 3/4 the transmission probability,

$$1 - p_{\text{liner}} = 0.04 + \frac{3}{4}T = 0.205 \tag{6.2}$$

where the factor of 3/4 is due to the liner layer being on only 3 sides of the wire. Here

---

[2]Semiclassically, one can think of an electron traveling ballistically in between bulk scattering events.

[3]In this picture, the introduction of transmission into Ta is a "bad deal" for Cu, because electrons entering Ta immediately lose their momentum, whereas those entering Cu from Ta have little net momentum. Still, reciprocity is maintained, as the introduction of the interface is a "good deal" from the point of view of Ta.

we use $1 - p$ for Cu as a crude approximation of the diffuse scattering for electrons reflected instead of transmitting at the interface.

We can also easily extend this analysis to consider thinner liner layers of thickness t_{Ta}. Recall from Chapter 3 that the relaxation time approximation is

$$\left(\frac{\partial f_k}{\partial t}\right)_{\text{collis}} = I \approx \frac{-(f_k - f_k^0)}{\tau},$$

so the cumulative scattering probability is Poisson:

$$P(s) = 1 - e^{-s/v_F \tau},$$

where we have converted from time to distance traveled s. Using the mean free path, we find

$$1 - p_{\text{liner}}(t) = 0.04 + \left(1 - e^{-2t_{\text{Ta}}/\lambda_{\text{Ta}}}\right)\frac{3}{4}T, \tag{6.3}$$

which interpolates smoothly between our insulator result and Eq. (6.2).

With $t_{\text{Ta}} > \lambda_{\text{Ta}}$, Eq. 6.1 gives a resistivity augmentation of about 13% for a 45 nm Cu square wire surrounded by Ta of at least $\sim$2 nm on three sides, or 4% for 45 nm Cu film with Ta on one surface. The thickness-dependence of this simple picture agrees well with the results of Rossnagel and Kuan [65], who measured sheet resistance of a 45 nm Cu film with $0 - 6$ nm of Ta deposited on it (note they use a film and deposit Ta on one surface). They find resistivity augmentation rapidly increasing to 10% for $\sim$2 nm of Ta, and leveling off for thicker layers (see Figure 6.3, which fits fairly well to an exponential falloff of form (6.3) with $\lambda_{\text{Ta}} \approx 2.2$ nm). Moreover, they find that resistivity decreases back to roughly the Cu-only value upon oxidation of the interface [65]. The elimination of the Ta conducting path actually improves conduction.

6.2.2 Discussion

However, as noted, our simple analysis gives only 4% resistivity augmentation compared with 10% observed by Rossnagel and Kuan [65]. We note first that the sheet resistance of 0.60 Ω/square reported in [65] is higher than the sheet resistance
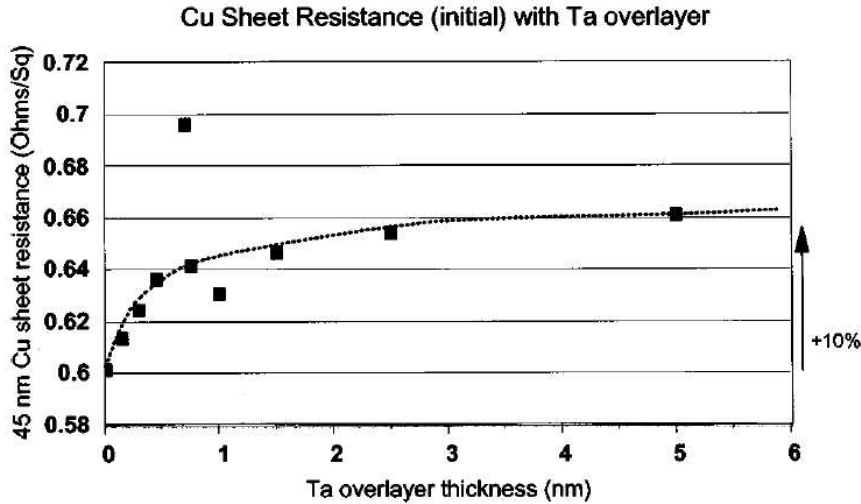
Figure 6.3: Increasing Cu sheet resistance as a function of Ta overlayer thickness. Note the leveling of the curve for Ta thicker than about 3 nm, or several Ta mean free paths. Figure taken from Ref. [65].

$1.7\mu\Omega \cdot \text{cm}/45$ nm $= 0.38$ Ω/square for bulk Cu, so there may be grain boundary scattering present also in the experiment. A possible reason for the quantitative disagreement on the magnitude of resistivity augmentation may be an underestimate in this work of the transmission probability across the interface. Resistivity augmentation of 10% for a single Ta overlayer would require an effective $1 - p \approx 0.6$, meaning that transmission probability should be closer to 60%. But it is also possible that the Cu/Ta epitaxy in real samples introduces greater interface disorder (roughness) than in our simulation system. Finally, it is possible that our assumption that reflection at the interface is 4% diffuse (based on our surface scattering work) underestimates the actual momentum loss at the Cu/Ta interface, and indeed this explanation is suggested by Rossnagel and Kuan [65]. A more detailed study of angular information on the reflected electrons at the interface would clarify this possibility, and we discuss our attempts to do so below.

Our result of $1 - p_{\text{liner}} = 0.20$ from Eq. (6.2) compares prominently against our

result of $1 - p \approx 0.04$ in Chapter 4. This is one of the primary conclusions of this work:

- **Interfaces with the liner layer are an important source of conductivity degradation.**

In the following sections, our goal is to improve this picture with more specific results on angle-dependent transmission and reflection at the interface.

6.3   Angle-Resolved Analysis

The remaining results of this chapter are preliminary, and we hope to refine them in a forthcoming publication[4].

Our simulation supercell in Cu contains 15 atoms in each of three layers, by contrast with the usual Cu (111) unit cell that contains just one atom in each of three layers. The ratio of supercell to unit cell volumes matches the ratio 15 of numbers of atoms. The need for this large supercell is due partly to the larger atomic volume of $\beta-$Ta compared to Cu, but mostly to the irregular crystal structure of $\beta-$Ta.

As a result, the Cu supercell Brillouin Zone is actually a reduced Brillouin Zone that has been folded over 15 times. The periodicity in our supercell (periodic boundary conditions transverse to the transmission direction) is roughly physical because real interfaces would contain a rough periodicity due to the heteroepitaxial match [41, 36, 43]. This periodicity enforces conservation of momentum in the transverse direction **up to a reciprocal lattice vector**.

Interpreting our simulation results is complicated by the fact that the transmission coefficients $T(k_x, k_y)$ can only be resolved up to equivalent (k_x, k_y) within the reduced Brillouin Zone. In order to extract the maximum information, we unfold

---

[4]In addition, I hope to finish a project with my committee member Prof. John Rehr, UW Physics, and his group to provide an alternative calculation of transmission by computing the Green's function in multiple scattering theory with FEFF [7].

the Brillouin Zone by Fourier transforming the transmission eigenstates over the Cu electrode supercell[5]. This task is also complicated by the unusual geometry of our Cu supercell. Given a state at the Fermi energy with k_x and k_y in the full Brillouin Zone, we can use the well-known Cu Fermi surface to compute k_z and hence the angle of incidence to the interface.

Our simulation is actually of transmission from Ta to Cu. But the coefficients $U_{L,i} \xrightarrow{t} U_{R,i}$ [11] become $U_{R,i} \xrightarrow{t^\dagger} U_{L,i}$ under time-reversal symmetry, so we can use our simulation for Cu to Ta transmission. In addition, even without time-reversal symmetry, total transmission $\bar{T} = \text{Tr}(t^\dagger t)$ is reciprocal because of the cyclical property of the trace [23] (see Eq. (3.21) and related discussion).

Then for each incoming state corresponding to a known mixture of k-points equivalent in the reduced Brillouin Zone, we know the transmission probability and something about the reflected and transmitted angles. Using this, we can extend our semiclassical analysis from above.

6.3.1 Analyzing Transmission States in the Reduced Brillouin Zone

In this section, we give details on "unfolding" the reduced Brillouin Zone.

Let us consider the problem in one dimension. Let us assume we have a supercell with dimension $L = ma$, where a is the lattice constant and m is an integer. The system is truly periodic over the distance a, but the simulation only knows about the periodicity (enforced by boundary conditions) over L. In general, the simulation allows us to set k in the reduced Brillouin Zone, so that

$$\psi(x + L) = e^{ikx}\psi(x) \tag{6.4}$$

---

[5]First we remove the $e^{i\vec{k}\cdot\vec{x}}$ dependence, where $k = (k_x, k_y)$ is a known vector in the reduced Brillouin Zone. This leaves us with a function periodic in the supercell. In general, the knowledge of the wavefunction values over a supercell n times larger than the unit cell will be enough information to find the coefficients of the n k-points equivalent to each other in the reduced Brillouin Zone. See Section 6.3.1.

with k in the reduced Brillouin Zone

$$\left(-\frac{\pi}{L}, \frac{\pi}{L}\right].$$

We have verified that Eq. (6.4) holds in our simulation output for the expected (two-dimensional) k value.

Let us define

$$\psi_P(x) \equiv e^{-ikx} \psi(x),$$

so that ψ_P is fully periodic over a supercell,

$$\psi_p(x + L) = \psi_p(x).$$

Then ψ_p may still be a linear combination of m possible Bloch functions (in a given band):

$$\psi_p(x) = \alpha_0 u_0(x) + \alpha_1 u_1(x) \exp\left(i\frac{2\pi x}{ma}\right) + \ldots + \alpha_{m-1} u_{m-1}(x) \exp\left(i\frac{2\pi x (m-1)}{ma}\right).$$

Here the $u_i(x)$ are periodic,

$$u_i(x + a) = u_i(x).$$

Knowing the wave function ψ_p over $L = ma$ gives us exactly enough information to solve for the m coefficients, $\alpha_0, \ldots, \alpha_{m-1}$. Defining

$$\omega \equiv e^{i\frac{2\pi}{m}},$$

we can write m equations for the m unknowns α_i, in the form:

$$\psi_p(na) = \alpha_0 u_0(0) \omega^{0 \cdot n} + \ldots + \alpha_{m-1} u_{m-1}(0) \omega^{(m-1)n},$$

for $n = 0, \ldots, m-1$. We will also need a little further information to find the $u_i(0)$, if we want to keep our Bloch functions normalized, and the α_i comparable. Note that we are not interested in $na < x < (n+1)a$ because we know that this can only give us information about the periodic u_i.

In practice, we do not attempt to solve this set of equations because we have a three-dimensional electrode, and there are small random errors in our simulation output that would introduce $y-$ and $z-$ dependence in our solutions for $x-$periodicity. Solving this set of equations by Gaussian elimination or other maximum-likelihood methods might be a good way to deal with these errors.

Instead, we Fourier transform to find the coefficients α_j. Intuitively, we expect that the probability $|\alpha_j|^2$ of being in the jth Bloch state is just the sum of probabilities of having the right phase shift over the distance a:

$$|\alpha_j|^2 = \sum_{n=0}^{\infty} \left| \langle \psi_P | \exp(i \frac{2\pi(n+j/m)}{a} x) \rangle \right|^2 . \qquad (6.5)$$

If all the u_i were constant, then of course the bracket above would just equal α_j for $n = 0$, and zero otherwise. But for general u_i, the higher Fourier coefficients of u_j can also contribute. In the following, we will fill in these details in our intuition and show that it is correct.

Continuing our discussion in one dimension, the Fourier transform of ψ_P will contain harmonics of the fundamental spatial frequency

$$k_0 = \frac{2\pi}{L} = \frac{2\pi}{ma},$$

and up to a maximal spatial frequency set by the mesh spacing δ of our real-space grid[6]:

$$k_{\max} = \frac{2\pi(N-1)}{L} = \frac{2\pi(N-1)}{N\delta} = (N-1)k_0,$$

where $L \equiv N\delta$. The Fourier tranform gives

$$\psi_P(x) = \sum_{j=0}^{N-1} \psi_{P,j} \, e^{i j k_0 x}. \qquad (6.6)$$

---

[6]Note that all the spatial frequencies 0, k_0, $\ldots$, $(N-1)\, k_0$ contain relevant information for a (complex) Fourier transform. Since ψ_P is periodic, we could do a Fourier *series* instead up to $\frac{N-1}{2}k_0$, but then we would still have both sine and cosine coefficients for each frequency.

We can also Fourier transform the $u_i(x)$ over the smaller interval a, with a higher fundamental frequency,

$$\frac{2\pi}{a} = \frac{2\pi}{L/m} = m\, k_0, \tag{6.7}$$

and the same maximal frequency,

$$k_{\max} = \frac{N-1}{m}\,(m\, k_0).$$

The transform gives:

$$u_n(x) = \sum_{j=0}^{\frac{N-1}{m}} u_{n,\,j}\; e^{i\, jmk_0\, x}. \tag{6.8}$$

Then

$$\psi_P(x) = \sum_{j=0}^{N-1} \psi_{P,\,j}\; e^{i\, j\, k_0\, x} = \sum_{n=0}^{m-1} \sum_{j'=0}^{\frac{N-1}{m}} \alpha_n\, \exp\left(i\frac{2\pi n x}{ma}\right) u_{n,\,j'}\; e^{i\, j'mk_0\, x}.$$

Noting that $\frac{2\pi n}{ma} = n\, k_0$, we see that

$$\psi_{P,j} = \sum_{n=0}^{m-1} \sum_{j'=0}^{\frac{N-1}{m}} \alpha_n\, u_{n,j'}\, \delta_{j,j'm+n}. \tag{6.9}$$

Given j, there is a *unique* way to write $j = j'm + n$ with n from 0 to $m-1$. Thus,

$$\psi_{P,j} = \alpha_n\, u_{n,j'}, \;\; j = j'm + n \tag{6.10}$$

with $j \le \frac{N-1-n}{m}$.

Substituting into Eq. (6.5), we get:

$$\sum_{j'=0}^{\infty} \left|\langle\psi_P|\exp(i\frac{2\pi(j'+n/m)}{a}x)\rangle\right|^2 = \sum_{j'=0}^{\infty} |\psi_{P,mj'+n}|^2 = |\alpha_n|^2 \sum_{j'=0}^{\infty} |u_{n,j'}|^2 = |\alpha_n|^2.$$

Of course $\sum_{j'=0}^{\infty} |u_{n,j'}|^2 = 1$, since the Bloch wave function must be normalized. We won't worry about the difference between summation up to N and ∞, since the validity of all our results depends on the mesh size δ being small.
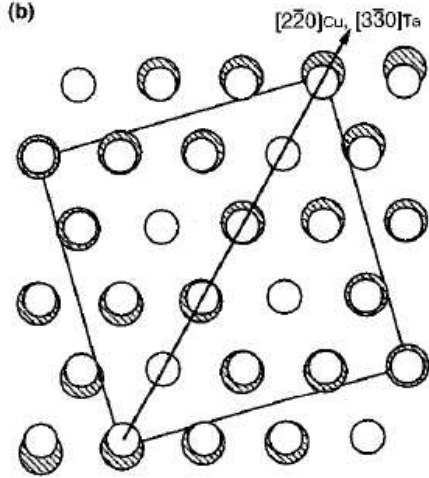
Figure 6.4: Epitaxial geometry between Ta (supercell shown as dark line) and Cu (111). Figure is taken from [41].

6.3.2 Two-dimensional considerations

In reality, we have a supercell with periodicity only in the plane perpendicular to the transmission direction, z (see Figure 6.4). There are 15 unit cells of Cu in the supercell (one unit cell for each atom in a (111) plane).

In two dimensions, we can use the same intuitive argument: the probability of finding the electron in a (2-dimensional) Bloch state is the sum of squared amplitudes to be in (plane wave) states that shift by the right phase under translation in the lattice. Each such amplitude is just the Fourier coefficient of ψ_P at a $\vec{k}$ connected to the $\vec{k}$ in the first Brillouin Zone by any reciprocal lattice vector.

We do a Fourier transform in only the two periodic dimensions x and y because the z dimension has the same periodicity as the Cu unit cell. Moreover, periodicity is only approximate (eventually we reach the interface) in the z dimension, so k_z is not conserved. This choice is a valid way to describe a wavefunction because k_x, k_y, and z commute, so one can define simultaneous eigenstates of them, $|k_x\, k_y;\, z\rangle$. Then

the probability

$$|\langle\psi|k_x\,k_y;\,z\rangle|^2 \tag{6.11}$$

to be in a given such state, like the probability to be in any well-defined quantum state, is a Hermitian observable[7]. This probability would be uniform in bulk, but in our case can show us how the system makes allowed transitions between (k_x, k_y) states through z.

Note, though, that this choice does change our 2-D reciprocal lattice vectors from their 3-D values. Let $\vec{X}$ and $\vec{Y}$ be the supercell lattice vectors (dark lines in Fig. 6.4). Then we can define the primitive lattice vectors $\vec{x}$ and $\vec{y}$ in Cu by

$$\vec{X} = 3\vec{x} + \vec{y}, \;\; \vec{Y} = 4\vec{y} - 3\vec{x},$$

as can be verified straightforwardly in the Figure. As the figure shows, $\vec{X} + \vec{Y} \propto [1\bar{1}0] \propto \vec{y}$, so one can also verify that $\vec{x} = \frac{a}{2}[0\bar{1}1]$, $\vec{y} = \frac{a}{2}[1\bar{1}0]$. Since $|\vec{x}|^2 = |\vec{y}|^2 = 2\vec{x}\cdot\vec{y}$, it follows that $|\vec{X}| = |\vec{Y}|$, even though the epitaxy requires $\vec{X} \cdot \vec{Y} = -|\vec{X}||\vec{Y}|/26$.

The third Cu primitive cell vector is not perpendicular to the plane shown, since the (111) planes are inequivalent. So normally the two reciprocal lattice vectors corresponding to $\vec{x}$ and $\vec{y}$ would have a component out of the plane. But here we have a supercell with only 2-D periodicity, and consider only a 2-D Fourier transform, so we use a 2-D reciprocal lattice:

$$\vec{b_1} = \frac{4}{3}\frac{2\pi}{a^2}(2\vec{x} - \vec{y}), \tag{6.12}$$

$$\vec{b_2} = \frac{4}{3}\frac{2\pi}{a^2}(2\vec{y} - \vec{x}). \tag{6.13}$$

In 2-D, the analysis is slightly complicated by the fact that the reciprocal lattice vectors for the supercell (reduced Brillouin Zone) are not proportional to the reciprocal lattice vectors for the Cu unit cell, which we now address.

---

[7]There is no violation of the Uncertainty Principle by implicitly measuring k_z through knowledge of k^2, since $|k_x\,k_y;\,z\rangle$ is not an energy eigenstate. But one can still take its overlap Eq. (6.11) with an energy state $|\psi\rangle$. We don't localize the electron while in energy eigenstate $|\psi\rangle$. We simply find the amplitude within this state for z to be entangled with (k_x, k_y).

Defining the supercell reciprocal lattice vectors $\vec{b_X}$ and $\vec{b_Y}$, we can write the Fourier transform of ψ_P,

$$\psi_P(\vec{r}) = \sum_{m,\,n=0}^{N-1} \psi_{P,\,m\,n}\, e^{i\,(m(\vec{b_X}\cdot\vec{r})+n(\vec{b_Y}\cdot\vec{r}))} \tag{6.14}$$

with $N\delta \approx |\vec{X}|$. Before we can re-write Eq. (6.5) in 2-D, we need a relationship for a general Fourier component in this sum,

$$\vec{k} = m\,\vec{b_X} + n\,\vec{b_Y} \equiv \beta_1\,\vec{b_1} + \beta_2\,\vec{b_2},$$

between periodicity in the supercell and in the Cu unit cell:

$$\vec{k}\cdot\vec{X} = 2\pi m = (\beta_1\vec{b_1} + \beta_2\vec{b_2})\cdot(3\vec{x}+\vec{y}) = (3\beta_1 + \beta_2)2\pi \;\Rightarrow\; 3\beta_1 + \beta_2 = m,$$

$$\vec{k}\cdot\vec{Y} = 2\pi n = (\beta_1\vec{b_1} + \beta_2\vec{b_2})\cdot(4\vec{y}-3\vec{x}) = (4\beta_2 - 3\beta_1)2\pi \;\Rightarrow\; 4\beta_2 - 3\beta_1 = n. \tag{6.15}$$

These equations give us a pair of simultaneous equations for the β:

$$15\beta_1 = 4m - n \equiv m', \quad 5\beta_2 = n + m \equiv n'. \tag{6.16}$$

Finally, we have the equivalent of Eq. (6.5). With our Fourier transform Eq. (6.14), we can sum over all reciprocal lattice vectors of the supercell, to within our spatial resolution $N\delta \approx |\vec{X}|$,

$$0 \leq m < N,\; 0 \leq n < N, \tag{6.17}$$

and can put the squared Fourier coefficients $|\psi_{P,\,m\,n}|^2$ in the probability $|\alpha_{j,\,j'}|^2$ for the appropriate Bloch state based on

$$j = m' \bmod 15, \quad j' = n' \bmod 5.$$

The result is

$$|\alpha_{j,\,j'}|^2 = \sum_{\{m,n\}:\;\; j=(4m-n)\bmod 15,\;\; j'=(m+n)\bmod 5} |\psi_{P,\,m\,n}|^2 \tag{6.18}$$
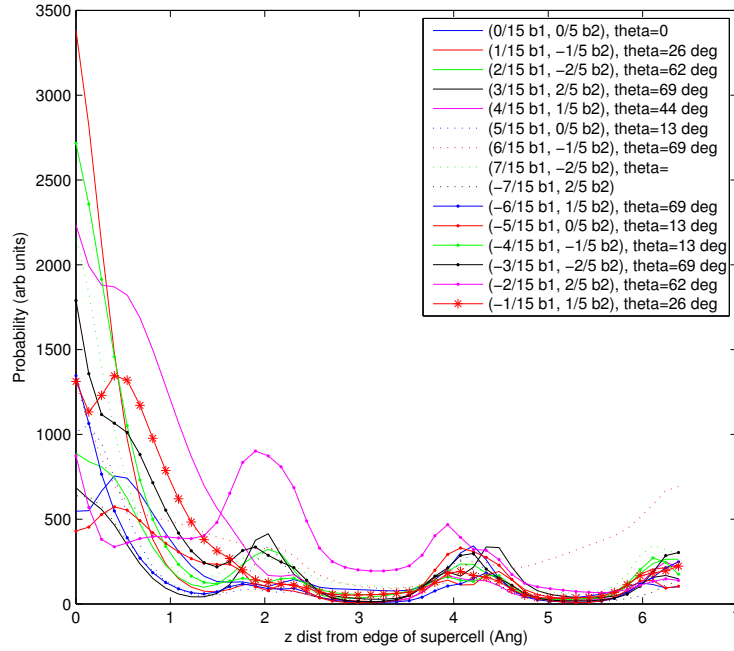
Figure 6.5: (Preliminary results). Example of transmission state analysis. Shown is probability to be in each Bloch state. The angle θ given is the polar angle of transmission, calculated by $\cos\theta \equiv \sqrt{k_x^2 + k_y^2}/k_F$. Recall that (k_x, k_y) relevant to θ should include the reduced-Brillouin Zone k-dependence in ψ in addition to the full Brillouin Zone dependence we found in ψ_P.

6.4 Angle-Resolved Results

An example of the transmission state analysis we developed in Sections 6.3.1 and 6.3.2 is shown in Figure 6.5. We have output from the Cu/Ta interface simulation for a whole set of eigenchannels (at (k_x, k_y) points covering the entire Brillouin Zone). We hope to analyze these soon to give transmission as a function of incident angles (θ, ϕ) relative to the interface.

Chapter 7

CONCLUSIONS

We have found that nanowire surfaces can be made sufficiently smooth with existing technology to reduce surface roughness scattering to manageable levels. Any process improvements on surface roughness should be focused on reducing the high-wavenumber tail of the PSD.

Grain boundary scattering is a significant source of resistivity for sufficiently small grain size. However, the damascene process can deposit interconnects with average grain size larger than the wire thickness, so grain boundary scattering can also be reduced but not eliminated. For thicker global interconnects, grain size may be as large as 300 nm or greater [25], so grain boundary scattering is unlikely to be a major contribution to global interconnect resistivity, and therefore to RC time delays. But for thinner local interconnects, grain size may be less than 50 nm [4], and therefore grain boundary scattering may be very relevant to power loss.

At an interface with a Ta liner layer, we find that electrons from Cu have a 22% probability of transmitting into Ta. Combining this with a Fuchs-Sondheimer-like model and an assumption about diffuse reflection at the interface, this yields an effective diffuse scattering parameter $1 - p = 0.2$ for sufficiently thick Ta liner layers. This is in semi-quantitative agreement with the experimental results of Rossnagel and Kuan [65] on Ta overlayers and nanofilms that interface only with insulators. Thus we conclude that scattering from liner layers is a major cause of conductivity degradation in Cu nanowires.

7.1 Quantitative importance of scattering mechanisms

Quantitatively, our calculations predict a resistivity augmentation of $\sim 5\%$ over bulk for global interconnects due to grain boundary scattering, 35% or more (assuming a conservative $R = 20\%$) for local interconnects due to grain boundary scattering, and 13% due to liner layer scattering. Observations of resistivity augmentation over 50% [20, 74] are typically for thin films deposited without the use of damascene process to control grain size, or have samples with small grain size despite using damascene [75]. These studies are therefore likely dominated by grain boundary scattering, and in most cases conclude so [20, 74]. In some cases, studies reporting very strong resistivity augmentation used Cu deposited on Ta [2], which could cause even more momentum loss at the interface.

We have concluded that scattering at rough interfaces with a dielectric is virtually negligible for RMS surface roughness in the range of $2 - 11$ Å measured experimentally [14, 61, 84], unless film thickness is less than $10 - 20$ nm. A few references [2] have measured samples with surface roughness as high as 4 nm, and therefore much higher than what we considered and what is probably present in interconnects. When these groups used samples with RMS roughness of 0.6 nm (closer to the range we considered in Chapter 4), they found $p \approx 1$, in agreement with our findings [2].

7.2 Recommendations

We recommend that processes such as the damascene process that keep grain size larger than wire thickness remain an important part of any attempts to scale interconnects. Any refinements in deposition processes should focus on increasing the grain size in local interconnects in order to limit the effect of grain boundary scattering on power loss.

For the liner layer, process improvements that limit transmission of electrons across the interface can improve conductivity. For example, a simple approach might be to

oxidize the liner layers after deposition of Cu. This would allow Ta to continue to function as a barrier to migration of Cu and seed layer for Cu deposition, but would limit momentum loss from scattering, as observed experimentally by Rossnagel and Kuan [65].

Surface roughness scattering is less important than the other mechanisms of conductivity degradation, but any process improvements should be focused on the high wavenumber tail (atomic scale roughness) of the Power Spectral Density.

BIBLIOGRAPHY

[1] *International Technology Roadmap for Semiconductors*, 2005.

[2] *J. Appl. Phys.*, 99:123705, 2006.

[3] *International Technology Roadmap for Semiconductors*, 2007.

[4] Evolution of cu microstructure and resistivity during thermal treatment of dama-scene line: Influence of line width and temperature. *Microelectronic Engineering*, 84(11):2723–2728, 2007.

[5] A. A. Abrikosov, L. P. Gorkov, and I. E. Dzyaloshinski. *Methods of Quantum Field Theory in Statistical Physics*. Dover Publications, 1975.

[6] Andrews. *Phil. Mag.*, 19:887–89, 1969.

[7] A. L. Ankudinov, B. Ravel, J. J. Rehr, and S. D. Conradson. Real-space multiple-scattering calculation and interpretation of x-ray-absorption near-edge structure. *Phys. Rev. B*, 58(12):7565–7576, Sep 1998.

[8] N. W. Ashcroft and N. D. Mermin. *Solid State Physics*. Brooks Cole, 1976.

[9] S. K. Bandyopadhyay and A. K. Pal. The effect of grain boundary scattering on the electron transport of aluminium films. *Journal of Physics D: Applied Physics*, 12(6):953–959, 1979.

[10] M. Brandbyge, J.-L. Mozos, P. Ordejón, J. Taylor, and K. Stokbro. *Phys. Rev. B*, 65:165401, 2002.

[11] M. Brandbyge, M. R. Sorensen, and K. W. Jacobsen. *Phys. Rev. B*, 56:14956, 1997.

[12] K. Capelle. *Brazilian J. of Phys.*, 36:1318–1343, 2006.

[13] F. Chen and D. Gardner. *IEEE Electron Device Lett.*, 19:508–510, 1998.

[14] K. Coffey and K. Barmak.

[15] M. P. Das and F. Green. *J. Phys: Condens. Matter*, 15:L687, 2003.

[16] S. Datta. *Electronic Transport in Mesoscopic Systems.* Cambridge University Press, 1995.

[17] S. Datta. *Nanotechnology*, 15:S433S451, 2004.

[18] de Vries. *J. Phys. F. Met. Phys.*, 17:1945–1952, 1987.

[19] J. W. C. de Vries. *Thin Solid Films*, 150(2-3):201–208, 1987.

[20] J. W. C. de Vries. *Thin Solid Films*, 167:25–32, 1988.

[21] N. M. Belyavskii E. I. Tochitskii. Grain-boundary electron scattering effect on metal film resistivity. *Phys. Status Solidi A*, 61(1):K21–K24, 1980.

[22] R. M. Feenstra, D. A. Collins, D. Z.-Y. Ting, M. W. Wang, and T. C. McGill. *Phys. Rev. Lett.*, 72:2749, 1994.

[23] Daniel S. Fisher and Patrick A. Lee. Relation between conductivity and transmission matrix. *Phys. Rev. B*, 23(12):6851–6854, Jun 1981.

[24] K. Fuchs. *Proc. Cambridge Philos. Soc.*, 34:100, 1938.

[25] R. H. Geiss and D. T. Read. Microstructure of 100 nm damascene copper overburden and lines. volume 6648, page 664808. SPIE, 2007.

[26] A. Gonis and W. H. Butler. *Multiple scattering in solids.* Springer, 2000.

[27] Gylfason. *Preprint to Thin Solid Films*, Oct 24, 2005.

[28] J. M. E. Harper, Jr. C. Cabral, P. C. Andricacos, L. Gignac, I. C. Noyan, K. P. Rodbell, and C. K. Hu. Mechanisms for microstructure evolution in electroplated copper thin films near room temperature. *Journal of Applied Physics*, 86(5):2516–2525, 1999.

[29] J. C. Hensel, R. T. Tung, J. M. Poate, and F. C. Unterwald. *Phys. Rev. Lett.*, 54(16):1840–1843, Apr 1985.

[30] K. Huang. *Statistical mechanics.* Wiley, 1987.

[31] Y. Imry, O. Entin-Wohlman, and A. Aharony. *Europhys. Lett.*, 72:263–269, 2005.

[32] A. Jiang, T. A. Tyson, L. Axe, L. Gladczuk, M. Sosnowski, and P. Cote.

[33] Q.-T. Jiang, M.-H. Tsai, and R. H. Havemann. In *Proc. IEEE International Interconnect Technology Conference, 2001*, pages 227–229, 2001.

[34] P. Kapur and J. P. McVittie. *IEEE Trans. Electron Devices*, 49:590–604, 2002.

[35] D. J. Keavney, S. Park, and C. M. Falco. *J. Appl. Phys.*, 91:8108, 2002.

[36] P. Klaver and B. J. Thijsse. *Mat. Res. Soc. Symp. Proc.*, 721, 2002.

[37] W. Koch and M. C. Holthausen. *A chemist's guide to density functional theory.* Wiley, 2001.

[38] W. Kohn. *Rev. Mod. Phys.*, 71, 1999.

[39] G. Kresse and J. Furthmller. *VASP the Guide.*

[40] G. Kresse and D. Joubert. From ultrasoft pseudopotentials to the projector augmented-wave method. *Phys. Rev. B*, 59(3):1758–1775, Jan 1999.

[41] K.-W. Kwon, C. Ryu, R. Sinclair, and S. S. Wong. *Appl. Phys. Lett.*, 71:3069, 1997.

[42] P. A. Lee and T. V. Ramakrishnan. *Rev. Mod. Phys*, 57:287, 1985.

[43] Y. Li and J. B. Adams. *Mat. Res. Soc. Symp. Proc.*, 721, 2002.

[44] H.-D. Liu, Y.-P. Zhao, G. Ramanath, S. P. Murarka, and G.-C. Wang. Thickness dependent electrical resistivity of ultrathin (¡40 nm) cu films. *Thin Solid Films*, 384(1):151–156, 2001.

[45] M. Marder. *Condensed Matter Physics.* Wiley-Interscience, 2000.

[46] A. F. Mayadas. *J. Appl. Phys.*, 39:4241.

[47] A. F. Mayadas, R. Feder, and R. Rosenberg. *J. Vac. Sci. Technol.*, 6:690, 1969.

[48] A. F. Mayadas and M. Shatzkes. *Phys. Rev. B*, 1:1382, 1970.

[49] A. F. Mayadas, M. Shatzkes, and J. F. Janak. *Appl. Phys. Lett.*, 14:345, 1969.

[50] A. Messiah. *Quantum Mechanics.* Dover Publications, 1999.

[51] A. E. Meyerovich and I. V. Ponomarev. *Phys. Rev. B*, 65:155413, 2002.

[52] A. E. Meyerovich and A. Stepaniants. *Phys. Rev. B*, 58:13242, 1998.

[53] A. E. Meyerovich and A. Stepaniants. *J. Phys.: Condens. Matter*, 12:5575, 2000.

[54] G. E. Moore. Cramming more components onto integrated circuits. *Electronics*, 38(8), 1965.

[55] M. Moseler, O. Rattunde, J. Mordiek, and H. Haberland. *Comp. Mat. Sci.*, 10:452–456, 1998.

[56] R. C. Munoz, C. Arenas, G. Kremer, and L. Moraga. *J. Phys.: Condens. Matter*, 15:L177–L184, 2003.

[57] I. Nakamichi. *J. Sci. Hiroshima Univ., Ser. A*, 54:49, 1990.

[58] Jong-Min Paik, Il-Mok Park, Young-Chang Joo, and Ki-Chul Park. Linewidth dependence of grain structure and stress in damascene cu lines. *Journal of Applied Physics*, 99(2):024509, 2006.

[59] M. Plischke and B. Birgersen. *Equilibrium statistical physics.* World Scientific, 2006.

[60] J. D. Plummer, M. D. Deal, and P. B. Griffin. *Silicon VLSI Technology: Fundamentals, Practice, and Modeling.* Prentice Hall, 2000.

[61] J. Purswani and D. Gall. *Thin Solid Films*, 516:465, 2007.

[62] M. H. Read and C. Altman. *Appl. Phys. Lett.*, 7:51, 1965.

[63] J. J. Rehr.

[64] F. Reif. *Fundamentals of statistical and thermal physics.* McGraw-Hill, 1965.

[65] S. M. Rossnagel and T. S. Kuan. *J. Vac. Sci. Technol. B*, 22:240, 2004.

[66] J. J. Sakurai. *Modern Quantum Mechanics.* Addison-Wesley Publishing Co., 1995.

[67] J. R. Sambles, K. C. Elsom, and D. J. Jarvis. *Phil. Trans. R. Soc. Lond. A*, 304(1486):365–396, 1982.

[68] M. A. Schneider, M. Wenderoth, A. J. Heinrich, M. A. Rosentreter, and R. G. Ulbrich. Current transport through single grain boundaries: A scanning tunneling potentiometry study. *Applied Physics Letters*, 69(9):1327–1329, 1996.

[69] M. A. Schneider, M. Wenderoth, A. J. Heinrich, M. A. Rosentreter, and R. G. Ulbrich. *J. of Elec. Mat.*, 26(4):383, 1997.

[70] S. B. Soffer. *J. Appl. Phys.*, 14:1710, 1967.

[71] S. B. Soffer. *Phys. Rev. B*, 2:3894, 1970.

[72] José M Soler, Emilio Artacho, Julian D Gale, Alberto García, Javier Junquera, Pablo Ordejón, and Daniel Sánchez-Portal. The siesta method for ab initio order-n materials simulation. *Journal of Physics: Condensed Matter*, 14(11):2745–2779, 2002.

[73] E. H. Sondheimer. *Adv. Phys.*, 1:1, 1952.

[74] W. Steinhögl, G. Schindler, G. Steinlesberger, and M. Engelhardt. Size-dependent resistivity of metallic wires in the mesoscopic range. *Phys. Rev. B*, 66(7):075414, Aug 2002.

[75] W. Steinhögl, G. Schindler, G. Steinlesberger, M. Traving, and M. Engelhardt. Comprehensive study of the resistivity of copper wires with lateral dimensions of 100 nm and smaller. *Journal of Applied Physics*, 97(2):023706, 2005.

[76] Z. Tesanovic. *J. Phys. C: Solid State Phys.*, 20:L829, 1987.

[77] Z. Tešanović, M. V. Jaric, and S. Maekawa. *Phys. Rev. B*, 57:2760–2763, 1986.

[78] V. Timoshevskii, Y. Ke, H. Guo, and D. Gall. *J. Appl. Phys.*, 103:113705, 2008.

[79] K. Tomizawa. *Numerical Simulation of Submicron Semiconductor Devices.* Artech House, Boston.

[80] N. Trivedi and N. W. Ashcroft. *Phys. Rev. B*, 35:6435, 1987.

[81] P. M. Th. M. van Attekum, P. H. Woerlee, G. C. Verkade, and A. A. M. Hoeben. Influence of grain boundaries and surface debye temperature on the electrical resistance of thin gold films. *Phys. Rev. B*, 29(2):645–650, Jan 1984.

[82] P. X. Xu, K. Xia, M. Zwierzycki, M. Talanana, and P. J. Kelly. Orientation-dependent transparency of metallic interfaces. *Physical Review Letters*, 96(17):176602, 2006.

[83] Q. G. Zhang, X. Zhang, B. Y. Cao, M. Fujii, K. Takahashi, and T. Ikuta. Influence of grain boundary scattering on the electrical properties of platinum nanofilms. *Applied Physics Letters*, 89(11):114102, 2006.

[84] W. Zhang, S. H. Brongersma, Z. Li, D. Li, O. Richard, and K. Maex. *J. Appl. Phys.*, 101:063703, 2007.

[85] W. Zhang, S. H. Brongersma, O. Richard, B. Brijs, R. Palmans, L. Froyen, and K. Maex. Influence of the electron mean free path on the resistivity of thin metal films. *Microelectronic Engineering*, 76(1-4):146–152, 2004.

VITA

Baruch Feldman received his undergraduate degree in Physics from MIT in 2001. He began the PhD program in Physics at the University of Washington in Seattle in 2003, and received a Master's degree in Physics in 2004. He joined Scott Dunham's Nanotechnology Modeling group in Electrical Engineering and does theoretical and computational research in applied condensed matter physics.

In addition to physics, Baruch has a love for issues relating to public affairs and policy. In between his Bachelor's and PhD, he did a Master's of Public Administration degree at City University of New York, graduating in 2003. He has also consulted for several nonprofit and international development organizations and acted as a research assistant in economics research.

Baruch believes strongly in science in the public interest, and hopes to combine his two loves throughout his career. His interests include science policy (in fields such as public investment in research, technology policy, clean technology, and alternative energy research), pure physics, and the applications of physics to technology.

Aside from his professional work, Baruch's other interests include tennis, running, and singing.